metals

Article

A Study of the Dynamic Mechanical Properties of Q460D Steel

Bo Huang [1,2], Li Lin [1,2], Tianli Xu [2,*], Xinke Xiao [3] and Jiuqiang Wang [4]

1. College of Civil Engineering and Architecture, Harbin University of Science and Technology, 52 Xuefu Road, Nangang District, Harbin 150080, China; 20b933068@stu.hit.edu.cn (B.H.); linli0119@163.com (L.L.)
2. School of Civil Engineering, Harbin Institute of Technology, 73 Huanghe Road, Nangang District, Harbin 150080, China
3. Henan International Joint Laboratory of Dynamics of Impact and Disaster of Engineering Structures, Nanyang Institute of Technology, 80 Changjiang Road, Wancheng District, Nanyang 473004, China; xinke@foxmail.com
4. Department of Mechanical Engineering, Harbin Engineering University, 145 Nantong Road, Nangang District, Harbin 150001, China; wangjiuqiang321789@163.com

* Correspondence: 19b933053@stu.hit.edu.cn

Abstract: The dynamic mechanical properties of Q460D steel were studied to facilitate an assessment of the impact resistance of building structures. In the present work, material performance tests of Q460D steel at different temperatures, strain rates, and stress states were conducted. Using a hybrid experimental–numerical approach, a modified Johnson–Cook (JC) constitutive relation, a modified Johnson–Cook (JC) fracture criterion, and a lode-dependent fracture criterion were calibrated. To validate the calibration, Taylor impact tests of Q460D steel rods onto rigid target plates were carried out in a one-stage light-gas gun system. Mushrooming, tensile splitting, and petalling failure modes were obtained as the impact velocity was increased from 191.6 to 422.1 m/s. A three-dimensional finite element model was built for the Taylor impact tests, and FE simulations were run using the material models calibrated. It was found that the FE simulations using the lode-dependent fracture criterion were reasonable in terms of the failure modes of the Taylor rods. In contrast, the fracture behavior of the Taylor rods was significantly underestimated using the lode-independent JC fracture criterion. Finally, the effect of anisotropy, strain rate sensitivity and yield plateau on the Taylor impact FE predictions were explored and discussed.

Keywords: lode parameter; taylor impact test; anisotropy; yield plateau; finite element simulation

Citation: Huang, B.; Lin, L.; Xu, T.; Xiao, X.; Wang, J. A Study of the Dynamic Mechanical Properties of Q460D Steel. *Metals* **2023**, *13*, 1609. https://doi.org/10.3390/met13091609

Academic Editor: Diego Celentano

Received: 2 August 2023
Revised: 3 September 2023
Accepted: 6 September 2023
Published: 18 September 2023

1. Introduction

In recent years, the impact resistance of building structures has become an active research field due to an increasing number of attacks. Q460 is a commonly used steel type in building structures (such as the Bird's Nest Olympic Stadium), and there is an urgent need for research on its dynamic material properties. Finite element (FE) simulations and supplementary tailored tests of particular exposed structural elements are usually employed for this purpose. The accuracy of FE simulations of impact events is evidently influenced by the material models utilized [1–11]. Hence, deep understanding and thorough characterization of materials' mechanical properties through elaborate material models play pivotal roles in research into local dynamic events in structures.

Material models may be distinguished into coupled and uncoupled models. Within coupled material models, it is assumed that the damage [12,13] accumulation process [14] affects the elastic and plastic properties of a material, while in uncoupled models, material yielding and fracturing are treated separately from each other [15]. The latter allows for an independent and therefore simpler calibration of the plasticity and fracture parts of a material model. Depending on a particular problem being solved and on the availability of relevant experimental data, the effects of a material stress state, strain rate, temperature, and other factors may be implemented into the plasticity and/or fracture parts of a material model, no matter whether it is coupled or uncoupled. As a result, despite their less sound physical basis, uncoupled models are much more popular in research and engineering practice [16–23].

Concerning plasticity models, to this date there exist over 200 various criteria for isotropic materials [24,25]. Among them there are elaborate versatile multiparameter three-invariant criteria with affine [26–28] and non-affine [29] octahedral cross-sections of a yield surface. Even the very first yield criteria, the so-called strength theories, were mainly two- or three-invariant:(1) maximum principal strain theory by Mariotte [30], Poncelet and de Saint-Venant [31]; (2) maximum principal stress theory by Galilei [32] and Rankine [33]; (3) criterion by Coulomb [34] generalized by Mohr [35]; (4) maximum shear stress theory by Tresca [36,37]; (5) specific elastic strain energy criterion by Beltrami [38]; (6) specific elastic distortion strain energy criterion by Maxwell [39], Huber [40], von Mises [41] and Hencky [42], which is commonly called simply the von Mises criterion, the designation that we will use within the present manuscript for brevity. Using linear transformations of the stress tensor, the technique applied for the first time (according to the authors' knowledge) by Sobotka [43], any isotropic criterion can be extended to an anisotropic case (see, for instance [44–46]). Furthermore, some accepted anisotropic yield criterions contain Hill48 [47], Yld2000-2d [48], BBC2000 [49] and Yld2000-18p [50] are proposed gradually. Applying a concept of the incubation time (see, for instance [51,52]) to the above mentioned yield criteria and, thus, turning from stress invariants in a criterion equation to stress impulse-like measures one can successfully describe plastic flow at very high strain rates in wide temperature ranges. Yet, a quick look through available literature over the past years related to FE simulations of impact interactions [53–63] reveals that, despite existence of all the above-mentioned elaborate criteria and techniques, the most widely used yield criterion has been and remains the von Mises one, in particular in the form proposed by Johnson and Cook (JC) [64]. The reason is not its limitless capabilities, but rather its ease of implementation and calibration.

Considering fracture criteria, one may emphasize two breakthroughs which determined directions of further development of the fracture mechanics in regard to numerical simulations of material fracture and a present state of the art. The first one is theoretical works by McClintock [65] and Rice and Tracey [66] and further experimental verification [67] of their results, which made it evident and universally recognized that an equivalent plastic strain at fracture of ductile materials exponentially decrease with the stress triaxiality increase. The second breakthrough is fracture experiments conducted by Bao [68] and further interpretation [69] of their results, which emphasized that fracture properties of ductile materials are in general dependent onto both the stress triaxiality and the Lode angle. Since that time several elaborate fracture criteria have been developed [70–73], but as in the case of the aforementioned elaborate yield criteria these and other advanced fracture criteria are not widely employed [61,74–78] even within uncoupled material models. The reason seems to be the same.

In light of the foregoing, great efforts are made to obtain relevant experimental data at different stress states, strain rates, and temperatures and calibrate at least uncoupled material models of various degree of complexity which are widely used in engineering practice. Very large amount of experimental data for 2024-T3(51) aluminum alloy is available in literature [60,64,68,79–85], In these works samples of various geometry (smooth and notched circular cylinders, thin flat "dog-bone" specimens, thin flat notched specimens, wide smooth and grooved plates, thin-walled tubes, thick-walled tubes, bars with square cross-sections, circular plates, plates with a circular hole, parallelepipeds, specimens with a butterfly-like gauge section, etc.) machined from different blanks (rolled sheets and plates of various thickness, large rolled blocks, extruded bars with circular or square cross-section, etc.) in different directions (through thickness of a plate, in a plane of a plate at 0°, 15°, 30°, 45°, 60°, 75°, 90° with respect to a rolling direction, etc.) are used in quasi-static (strain rates from 10^{-4} s^{-1} to 1 s^{-1}) and dynamic (on Split Hopkinson Bar-type test facilities with strain rates up to 10^{4} s^{-1}) tests of various types (tension, compression, torsion/shear, combined torsion-compression and torsion-tension/shear-tension, bulge test, biaxial compression, etc.) conducted at different temperatures (from −50 °C to 450 °C) and under proportional or non-proportional (pre-tension, pre-compression, pre-torsion, etc.) loading to identify anisotropy of a material yield stress, strain hardening law, strain rate and temperature effects onto material yielding, stress state dependence of the material yielding and construct a material fracture locus in a mixed stress-strain space at different strain rates, temperatures and loading conditions. In most of the mentioned works obtained experimental data has been used to calibrate a particular material model. And, of course, one may simultaneously use several different sources for calibration, like it was done in [86] to calibrate a proposed three-invariant yield criterion, in [87] to calibrate the three-invariant fracture criterion by [71], and in [88] to calibrate a proposed three-invariant fracture criteria. However, most of structural metals and alloys, in particular steels commonly used in civil engineering, are not so "popular" within the research community and not very much experimental data is available for these materials. Yao et al. [89] analyzed the cyclic elastoplastic response of Q235B steel, the effect of Lode dependence of the plasticity response of structural steel Q235 is investigated. Yang et al. [90] investigated a strain rate sensitivity of S690 structural steel, determined parameters of the strain rate hardening laws introduced, respectively, by Cowper and Symonds [91] and Johnson and Cook [92]. Jiang et al. [93] proposed a prediction formula for ultimate bearing capacity of Q690 built-up K joints. Tian et al. [94] provided a novel steel frame joints with corrugated plates to improve the collapse resistance of Q235B steel frame structures. Based on Q345B steel, the "false steel-concrete composite structures" was proposed and the seismic performance of it was analyzed by Huang et al. [95]. Xiao and his coworkers simulated the failure process of 316L austenitic stainless steel [61], Ti-6Al-4V Alloy [96] and 6061-T651 Al [97] target plates that were impacted by blunt rigid projectiles using the Lode-dependent MMC, Lou fracture criterion, and Lode-independent JC fracture criterion and analyzed the effect of the Lode parameter on the prediction of the ballistic limit velocity in FE simulations. Hence, compared to the Lode-independent fracture criteria, the prediction accuracy of FE simulations for Taylor impact or ballistic tests was effectively improved by incorporating the Lode parameter.

At present, research on the dynamic material properties of typical structural steels incorporating the lode parameter is relatively limited. In this study, a modified Johnson–Cook (JC) constitutive relation, a modified Johnson–Cook (JC) fracture criterion, and a lode-dependent fracture criterion were applied to describe, respectively, the flow stress and fracture behavior of Q460D steel. The model parameters were calibrated by conducting material performance tests of Q460D steel at different temperatures, strain rates, and stress states, and using a hybrid experimental-numerical method. To validate the calibration, a Taylor impact test was performed, and the mushrooming, tensile splitting, and petalling failure modes of the projectile were obtained. A three-dimensional finite element model was built for the Taylor impact tests, and FE simulations were run using the material models calibrated. The simulation results of the two fracture criteria were compared with the results observed in the experiment, and the prediction capabilities of the two fracture criteria were compared. It was found that the fracture behavior of the Q460D steel has a significant lode correlation. Then, the effect of the material property representation on the prediction accuracy in FE simulations was examined and discussed.

2. Material Model and Calibration

2.1. Material Model

The JC constitutive relation [64], which is commonly used in engineering practice, was applied to characterize the equivalent plastic strain in the material model. However, in the study of the dynamic material properties of typical structural steels, Lin et al. [98] found that the thermal softening behavior cannot be well captured by the JC constitutive relation. To improve the prediction accuracy, the original temperature item was modified by adding a thermal softening coefficient F. Meanwhile, based on the method inspired by Sung et al. [99] , Xiao et al. [100] modified the strain hardening term of the JC constitutive relation, by substituting the Ludwik law [101] with a linear combination of the Ludwik and Voce laws [102] To include the effect of the thermal softening and strain hardening, a modified Johnson–Cook (MJC) constitutive relation that combined the two types of modifications was adopted, expressed as follows:

$$\sigma_{eq} = \{\alpha(A + B\varepsilon_{eq}^{n}) + (1-\alpha)[A + Q(1 - e^{-\beta\varepsilon_{eq}})]\}(1 + C\ln\dot{\varepsilon}^{*})(1 - FT^{*m}), \quad (1)$$

where A, B, n, α, Q, and β are the strain hardening coefficients; C is the strain rate sensitivity coefficient; F and m are the thermal softening coefficients; $\dot{\varepsilon}^{*} = \dot{\varepsilon}/\dot{\varepsilon}_0$, $\dot{\varepsilon}_0$ and $\dot{\varepsilon}$ are the equivalent plastic strain, the dimensionless plastic strain, the reference strain rate, and the strain rate, respectively; and $T^{*} = (T - T_{\mathrm{r}})/(T_{\mathrm{m}} - T_{\mathrm{r}})$, T, T_{r}, and T_{m} are the homologous temperature, the material temperature, the reference temperature, and the melting point, respectively. Furthermore, the adiabatic assumption was adopted at a high strain rate, and the temperature rise ΔT can be defined as follows:

$$\Delta T = \frac{\chi}{\rho C_{\mathrm{p}}}\int \sigma_{eq}\mathrm{d}\varepsilon_{eq}, \quad (2)$$

where χ is the Taylor–Quinney coefficient, which is usually assumed to be 0.9, and ρ and C_{p} are the material density and the specific heat, respectively.

The fracture strain was expressed by the JC and the Lode-dependent EJMA fracture criteria. The JC fracture criterion is widely applied in engineering practice due to its comprehensive consideration of the stress triaxiality, strain rate, and temperature. To well characterize the thermal softening effect, Xiao [103] added a thermal softening coefficient D_6 in the original temperature item, and it can be expressed as follows:

$$\varepsilon_f = [D_1 + D_2\exp(D_3\sigma^{*})](1 + D_4\ln\dot{\varepsilon}^{*})(1 + D_5T^{*D_6}), \quad (3)$$

where D_1, D_2, D_3, D_4, D_5, and D_6 are all material constants, and σ^{*} is the stress triaxiality defined by $\sigma^{*} = \sigma_{\mathrm{m}}/\sigma_{eq}$, where σ_{m} is the hydrostatic pressure given by $\sigma_{\mathrm{m}} = (\sigma_{11} + \sigma_{22} + \sigma_{33})/3$. The damage indicator can be defined as follows:

$$D = \sum\frac{\Delta\varepsilon_{eq}}{\varepsilon_f}, \quad (4)$$

where $\Delta\varepsilon_{eq}$ is the equivalent plastic strain increment.

In studies of the fracture behavior of metals in different stress states, the effects of the stress triaxiality and the lode parameter, which is determined by the third invariant of the deviatoric stress tensor, should be considered, especially at low stress triaxialities. The lode angle θ is defined as:

$$\xi = \cos(3\theta) = \frac{3\sqrt{3}}{2}\frac{J_3}{J_2^{2/3}}, \quad (5)$$

where J_2 and J_3 are the second and third invariants of the deviatoric stress tensors, $0 < \theta < \pi/3$, and $-1 < \xi < 1$. The relationship between the lode parameter L and lode angle θ can be expressed as follows:

$$\overline{\theta} = 1 - \frac{6\theta}{\pi} = 1 - \frac{2}{\pi}\arccos(\xi) = 1 - \frac{2}{\pi}\arccos(\frac{r}{q})^{3}, \quad (6)$$

$$r = [\frac{27}{2}(\sigma_1 - \sigma_{\mathrm{m}})(\sigma_2 - \sigma_{\mathrm{m}})(\sigma_3 - \sigma_{\mathrm{m}})]^{1/3}, \quad (7)$$

$$q = \sqrt{\frac{1}{2}(\sigma_1 - \sigma_2)^2 + (\sigma_2 - \sigma_3)^2 + (\sigma_3 - \sigma_1)^2}, \quad (8)$$

$$L = \frac{3\tan\theta - \sqrt{3}}{\tan\theta + \sqrt{3}}, \quad (9)$$

where σ_i represents the first, second, and third main stresses when i = 1, 2, and 3, respectively.

Thus, the lode parameters θ, $\overline{\theta}$ and L can be inferred when one is known. Due to its more concise expression for L, the EJMA fracture criterion, which is characterized by lode parameter L, was adopted. Combined with the expression of the strain rate and temperature in the MJC fracture criterion, the equivalent plastic strain can finally be defined as follows:

$$\varepsilon_{eq} = \frac{C_3}{\left[\left(\frac{2}{\sqrt{L^2+3}}\right)^{C_1} + \left(\eta - \frac{1}{3}\right)\right]^{C_2}}(1 + D_4 \ln \dot{\varepsilon}^*)(1 + D_5 T^{*D_6}), \quad (10)$$

where C_i (i = 1, 2, or 3) and η are the material constants and stress triaxiality, respectively.

2.2. Calibration of the MJC Constitutive Relation

To obtain the strain term parameters of the MJC constitutive relation, quasi-static tensile tests were conducted using a SHIMADZU AG-X Plus electronic universal testing machine at the Nanyang Institute of Technology, and an SHIMADZU SIE-560SA Automatic extensometer was used to record the test data. The tensile speed was 2 mm/min, and the gauge length was 25 mm. The specimen dimensions are shown in Figure 1a. Additionally, all of the specimens in this paper were processed using a Q460D steel plate (length × width × thickness = 500 mm × 500 mm × 30 mm), the chemical components of which are listed in Table 1.

Table 1. Chemical composition of the Q460D steels (mass fraction, %).

C	Si	Mn	P	S	Al	Nb	V	Ti	Cr	Ni	Cu	Mo	B	N
0.13	0.3	1.4	0.014	0.002	0.03	0.031	0.043	0.014	0.03	0.01	0.02	0.01	0.0002	0.0032

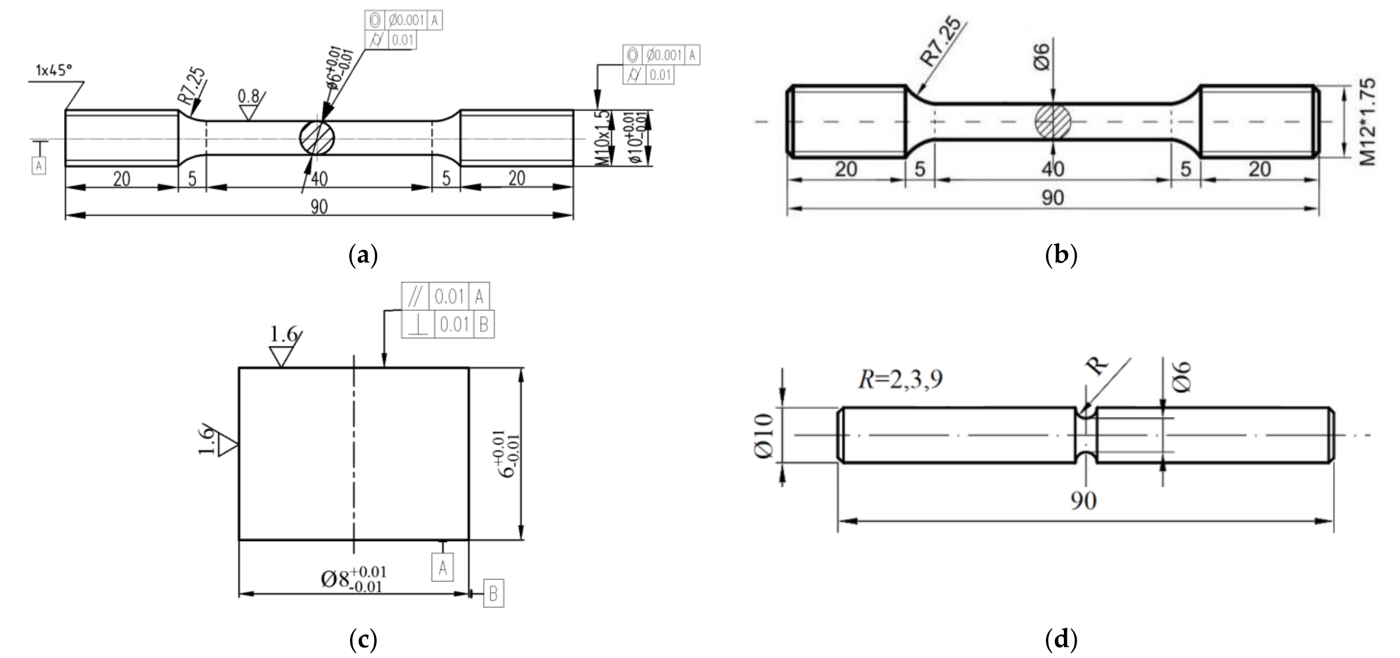

Figure 1. *Cont.*

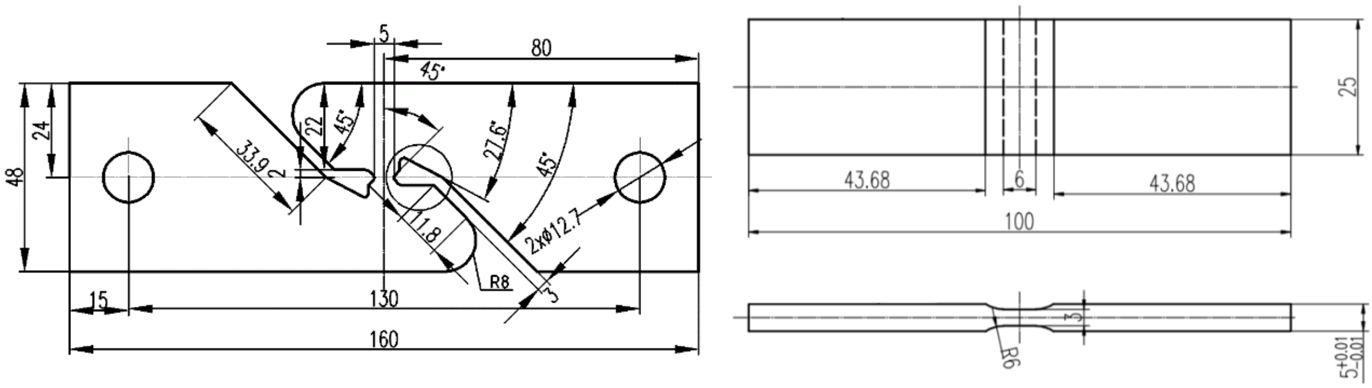

(**e**) (**f**)

Figure 1. Specimens used in the mechanical test (mm): (**a**) Smooth round bar; (**b**) High-temperature or dynamic tension; (**c**) Dynamic compression; (**d**) Round notched bar; (**e**) In-plane shear; (**f**) Plane stress.

The engineering stress–strain curves of each smooth test (ST) are shown in Figure 2. The yield strength was derived from the lower yield point in the yield plateau. The average of each test was A = 434.63 MPa, and the elastic modulus was 210.351 GPa. The curve from the yield plateau to the necking point in the true stress–strain curve was intercepted and fitted using Origin software, based on a linear combination of the Ludwik and Voce laws. The fit parameters were as follows: B = 666.54 MPa, n = 0.57726, Q = 217.61 MPa, and β = 16.819.

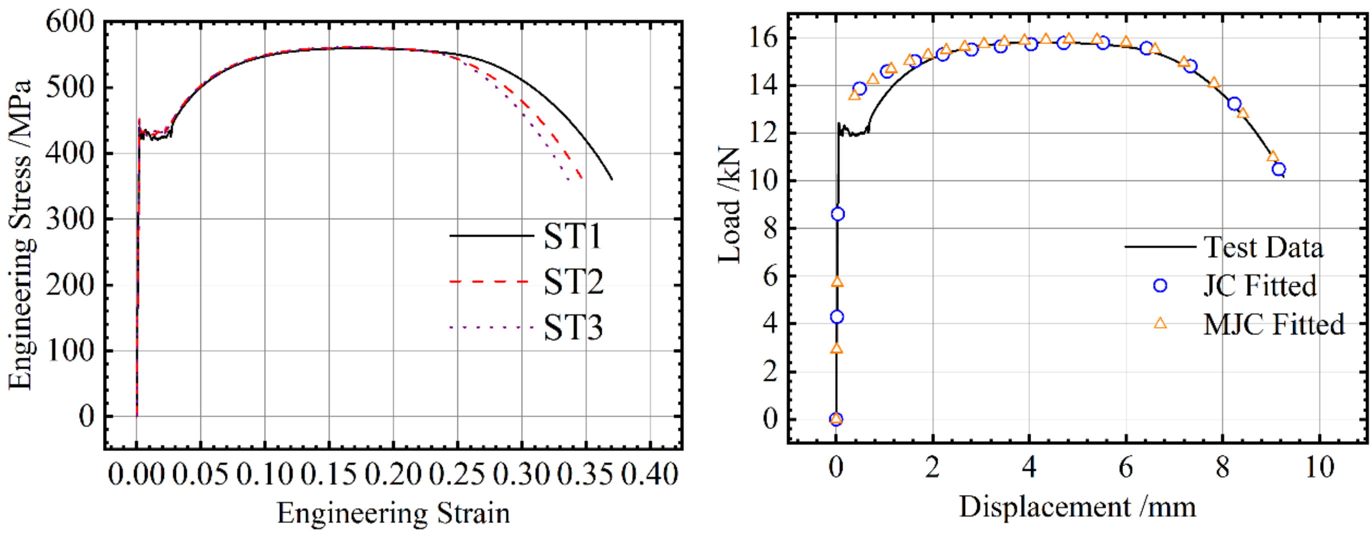

(**a**) (**b**)

Figure 2. Test and numerical analysis results of a smooth tensile test: (**a**) Engineering stress–strain curves; (**b**) Curve obtained through numerical analysis.

To confirm the value of α in Equation (1) and verify the calibration, a 2D axisymmetric model was established using ABAQUS finite element software. The element size in the gauge section was 0.1 mm × 0.1 mm, and that outside the gauge section was 0.1 mm × 0.3 mm. Each strain parameter obtained above was input into the FE simulation using a tabular method [103], and the value of α was varied until the load–displacement curve of the numerically simulated result was similar to the test result, as shown in Figure 2b, and the value of α was 0.85.

The strain rate parameters were calibrated via dynamic tensile tests and split-Hopkinson pressure bar (SHPB) tests. Dynamic tensile tests were conducted using a universal test machine with an automatic extensometer, and the specimen size is shown in Figure 1b. The gauge length was 25 mm. Four tensile speeds from 200 to 800 mm/min were tested, and the engineering stress–strain curves are shown in Figure 3.

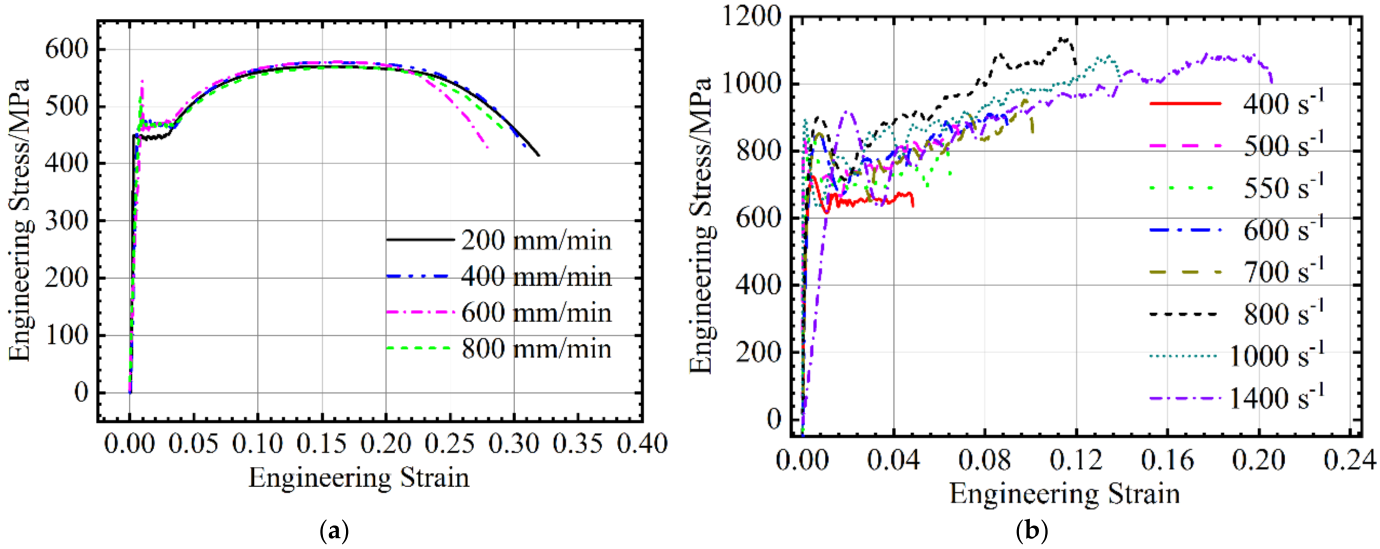

Figure 3. Dynamic test results: (**a**) Engineering stress–strain curves of dynamic tensile tests; (**b**) Engineering stress–strain curves of SHPB tests.

The SHPB test was conducted using the SHPB apparatus shown in Figure 4. The apparatus mainly included a striker bar, incident bar, transmitter bar, and absorber bar, all of which were made of 18Ni (350) high-strength steel and had 12 mm diameters. The length of the striker bar was 300 mm, and lengths of the other bars were all 1000 mm. The specimens had an 8 mm diameter and a 6 mm height, as shown in Figure 1c. One or two tests were conducted for each strain rate. The signals from the incident bar and transmitter bar were processed to obtain the engineering stress–strain curves at different pressures, as shown in Figure 3b. Oscillations are evident in stress–strain data at the highest strain rate, which is a very common phenomenon caused by the initial data being obtained while the system is not at equilibrium.

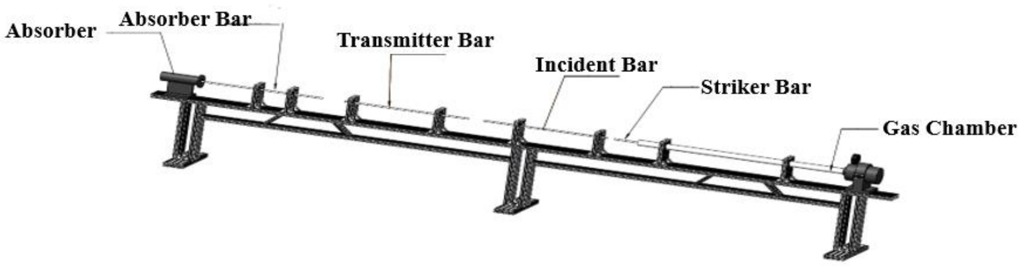

Figure 4. Schematic diagram of split-Hopkinson pressure bar.

The plastic and elastic sections in the engineering stress–strain curves of SHPB test were fitted, and the value of the intersection point was taken as the yield strength. Meanwhile, this was combined with the yield strength, which was taken from the lower yield point in the yield plateau of the dynamic tensile test, with the reference strain rate as 8.333×10^{-4} s^{-1}, which derived from the smooth tensile test. The strain rate coefficient was calibrated using the least squares method, as shown in Figure 5, and it was determined that C = 0.0404.

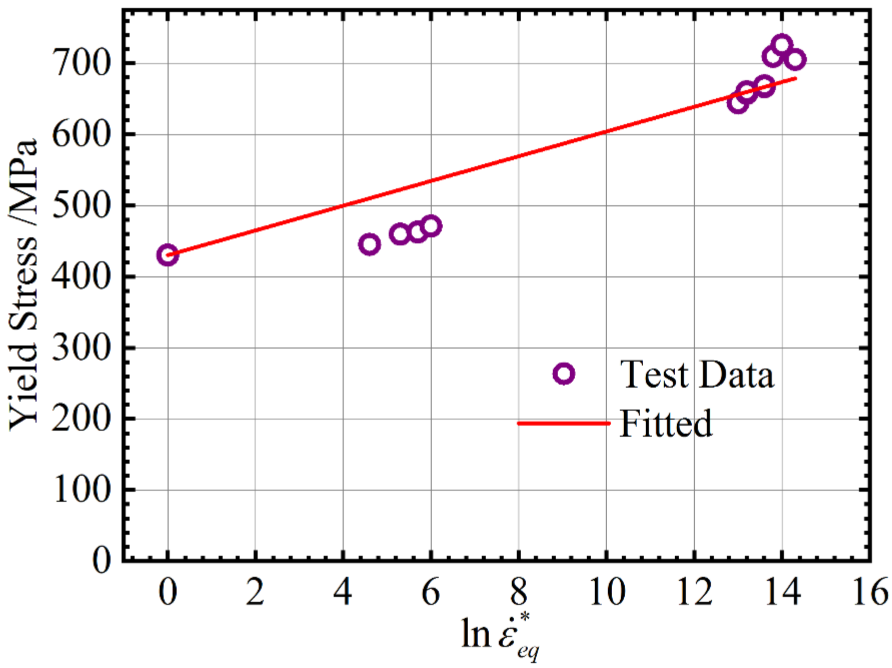

Figure 5. Yield stress of Q460D steel at various strain rates.

Due to the relatively high melting point of Q460D steel, four temperature gradients from 300 to 900 °C were established to study the material's properties at different temperatures. The test was conducted using a universal testing machine with a high-temperature furnace and a temperature control system at the Harbin Institute of Technology. The specimen dimensions are shown in Figure 1b. However, at a temperature of 900 °C, the specimen was softened more significantly and became embedded in the fixture. Consequently, the specimen was hard to remove, and damaged the fixture. Hence, only one test was conducted at this temperature. Finally, the engineering stress–strain curves at different temperatures were obtained, as shown in Figure 6.

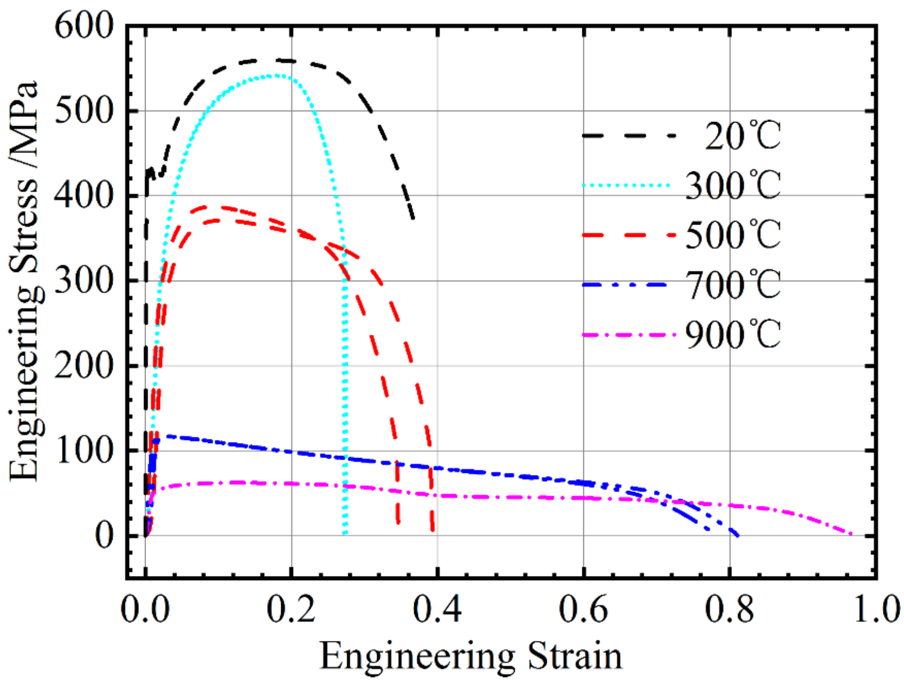

Figure 6. Engineering stress–strain curves of the tensile tests at different temperatures.

Figure 6 shows that the yield and tensile strengths decreased gradually as the temperature increased, and the material exhibits a significant thermal softening effect [104]. At temperatures of 20 and 300 °C, the yield strength was derived from the lower yield point of the yield plateau. At temperatures from 500 to 900 °C, the yield strength was determined from the stress, which corresponded to a 0.2% strain. A dimensionless temperature parameter was defined as $T^* = (T - T_r)/(T_m - T_r)$, where the melting point of Q460D steel is T_m = 1800 K and the reference temperature was T_r = 293 K. Based on the relationship between the yield strength and T* under different temperature conditions, the parameters of the temperature term of the MJC in Equation (1) were fitted using Origin software, as shown in Figure 7. The values were F = 1.777 and m = 1.228.

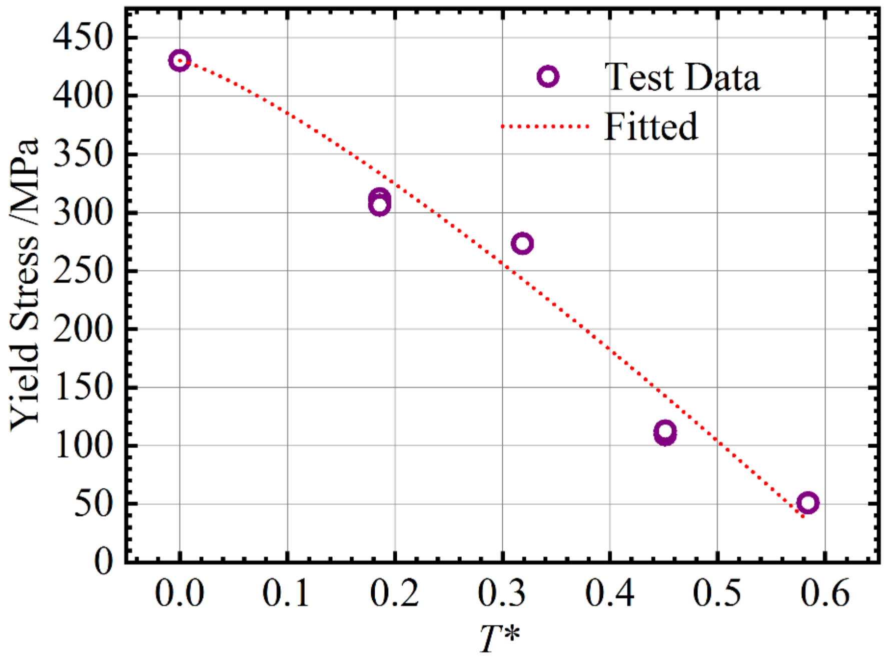

Figure 7. Yield stress of Q460D steel at various temperatures.

2.3. Calibration of the Fracture Criterion

The stress state was studied from various perspectives, including high-stress triaxiality, low-stress triaxiality, and plane strain. Notched tensile tests were performed using radii of 2, 3, and 9 mm. In-plane shear and plane strain tests were conducted on the universal test machine at the tensile speed of 0.5 mm/min. The specimen dimensions are shown in Figure 1d. Matte white undercoats and matte black speckles were printed on the specimen surfaces.

Full-surface deformation was recorded using an optical measurement system provided by Correlated Solution Inc. (Vic2D 2009, Columbia, SC, USA), and the relative elongation between the two gauge points was recorded using the virtual extensometer option in the DIC (digital image correlation) system. A centered single CCD (charged couple device) camera was used to collect test photos in the notched tensile tests, and the gauge length was 25 mm. Front- and rear-facing double CCD cameras were used for the in-plane shear tests to capture the complex deformation behavior, and the gauge length was 30 mm. A three-dimensional (3D) double CCD camera method was used for the in-plane stress tests, as shown in Figure 8. After the tests, MatchID-2D and MatchID-3D software were used to extract the deformation and strain fields from the recorded pictures; the test results are shown in Figures 9 and 10.

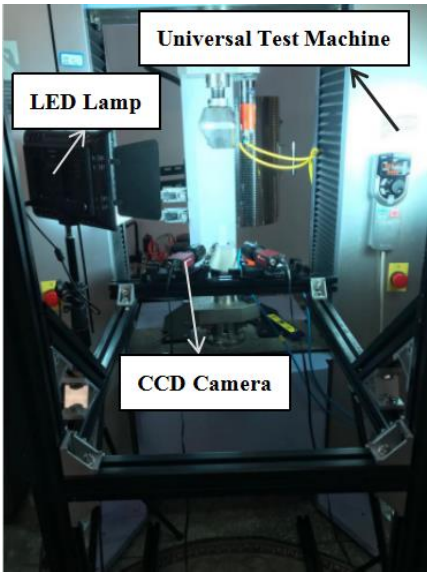

Figure 8. Photograph of the plane strain tensile test setup.

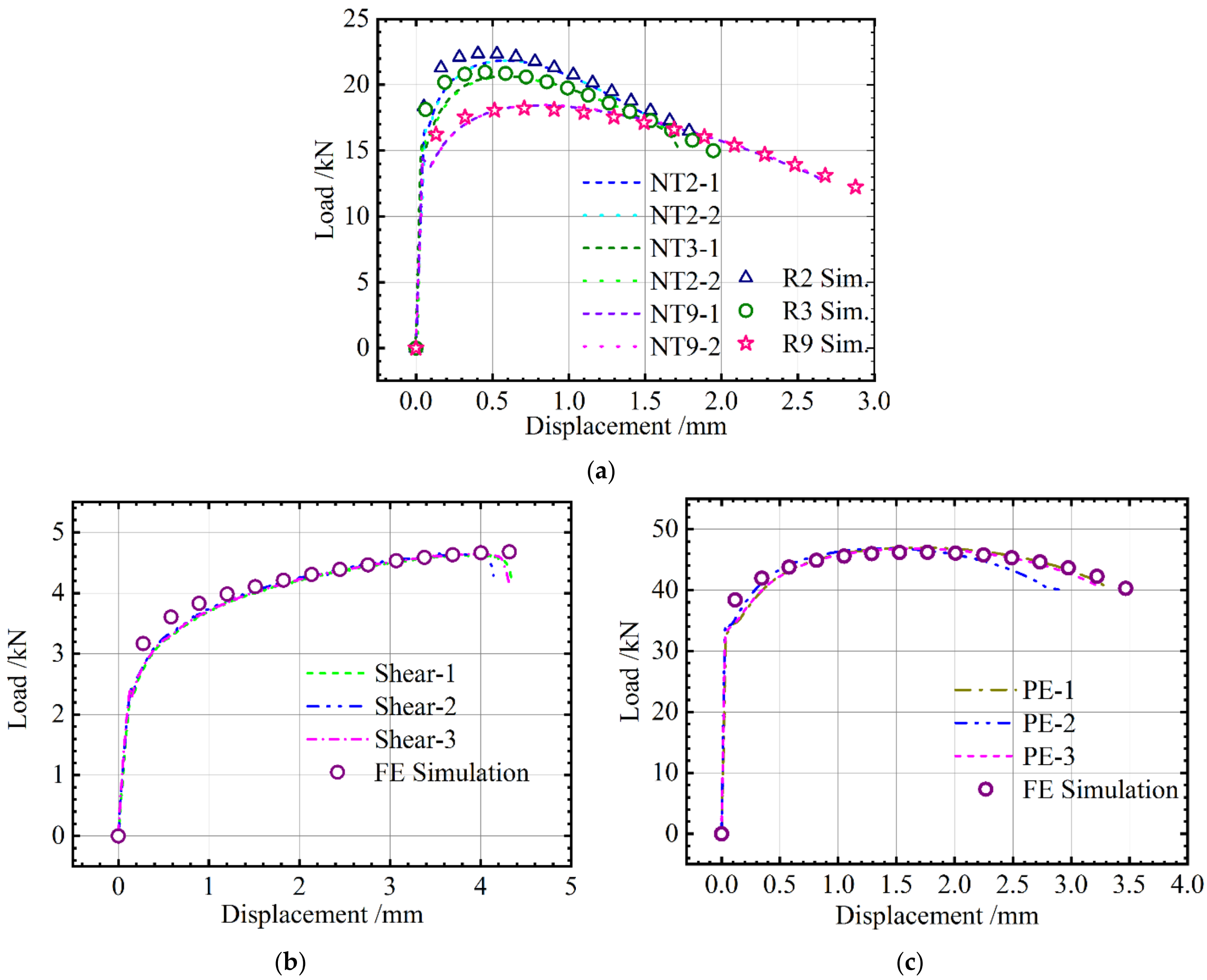

Figure 9. Force–displacement curves for several mechanical tests: (**a**) Round notched test; (**b**) In-plane shear test; (**c**) Plane stress.

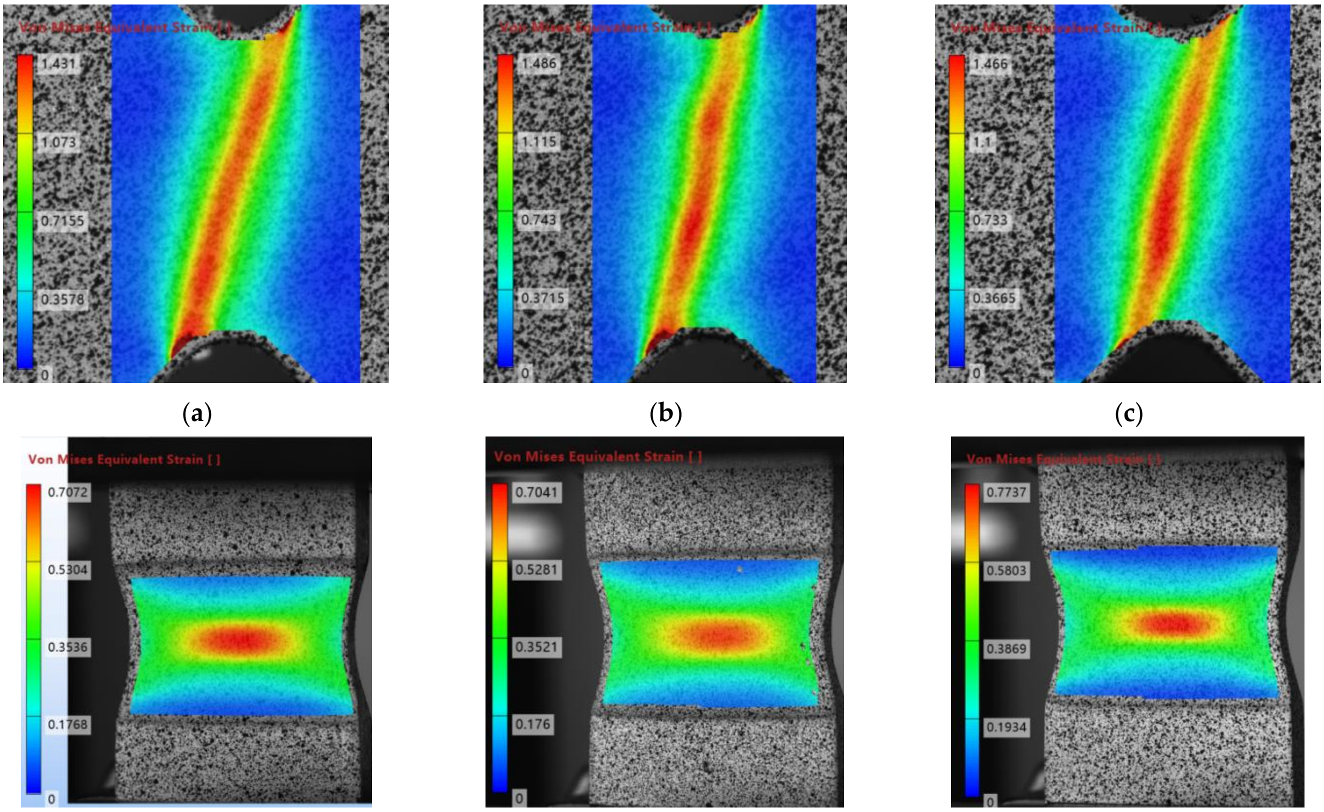

(**d**) (**e**) (**f**)

Figure 10. Surface strain of in-plane shear and plane stress test: (**a**) Shear-1; (**b**) Shear-2; (**c**) Shear-3; (**d**) Plane stress-1; (**e**) Plane stress-2; (**f**) Plane stress-3.

Due to the irregularity of the fracture surfaces of the recovered fractured specimens, measurement errors of the fracture area were obtained. The stress triaxiality value was not invariant during the deformation and fracture process. Hence, the fracture properties of each test should be examined through FE simulations. Numerical models were established in ABAQUS. A two-dimensional (2D) axisymmetric model was established to simulate the notched tensile tests. The element size in the gauge section was 0.1 mm × 0.1 mm, and that outside the gauge section was 0.1 mm × 0.3 mm. A 3D model was established for the in-plane shear and plane stress tests. The element size in the gauge section was 0.1 mm × 0.1 mm × 0.1 mm, and increased gradually closer to the edge, as shown in Figure 11.

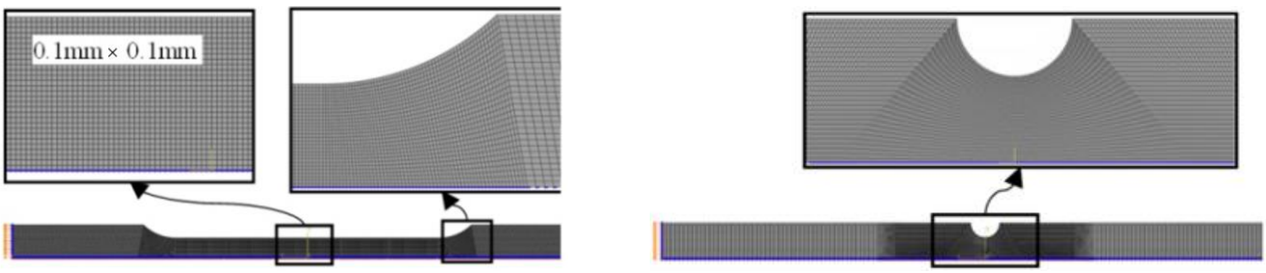

(**a**) (**b**)

Figure 11. *Cont.*

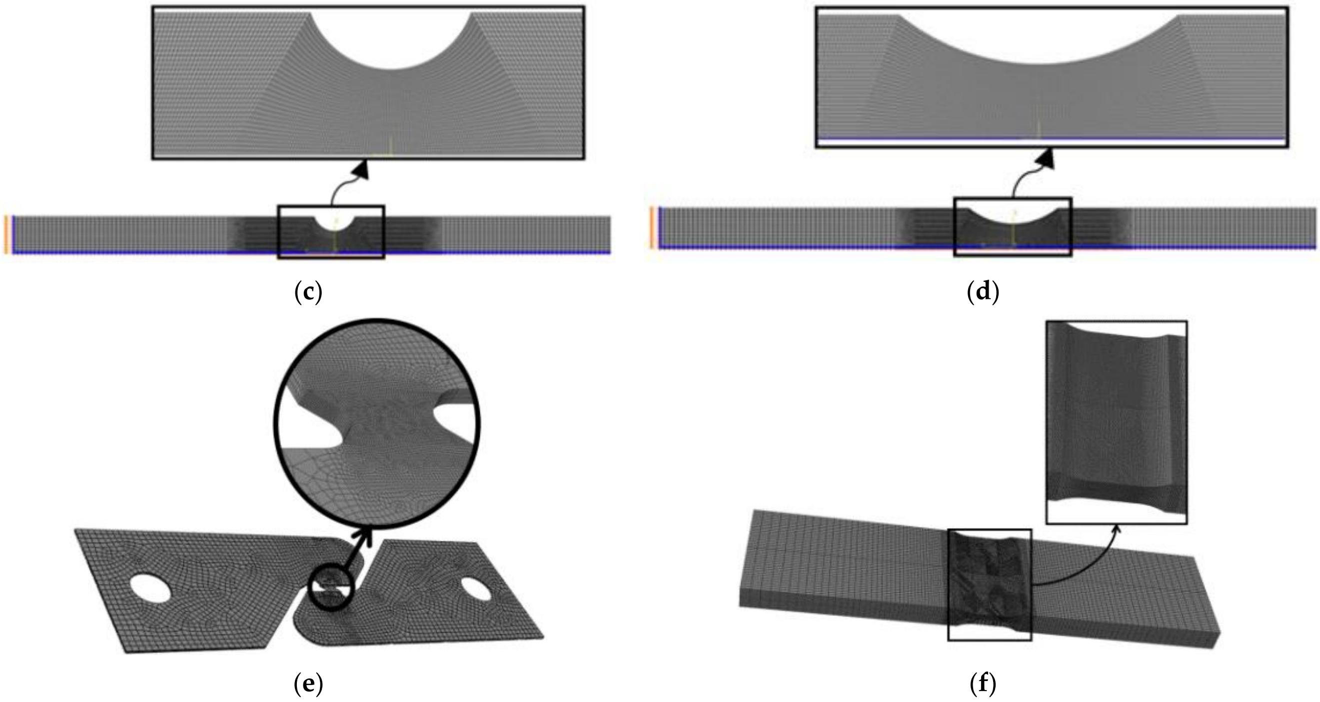

Figure 11. Numerical model of each mechanical test: (**a**) Smooth round bar; (**b**) R = 2; (**c**) R = 3; (**d**) R = 9; (**e**) In-plane shear; (**f**) Plane stress.

There was slight error between the experimental and simulated force–displacement curves for the in-plane shear test, which illustrated the effect of the lode angle on the plastic flow behavior of Q460D steel. The correction coefficient was adjusted until the simulated curve overlapped with the experimental curve, and the current α value in Equation (1) was 0.35.

Because the numerical results were similar to the test results, the fracture strain from the numerical simulation, i.e., the equivalent plastic strain (PEEQ) at the moment of fracture, can be used directly, as shown in Figure 12. The equivalent plastic strain at the edge of the gauge section was slightly higher than that at the center. The stress state at the edge section was a pressure condition, and that in the center was a shear condition. Thus, the fracture occurred more easily in the center section, and the edge section was not considered in the analysis.

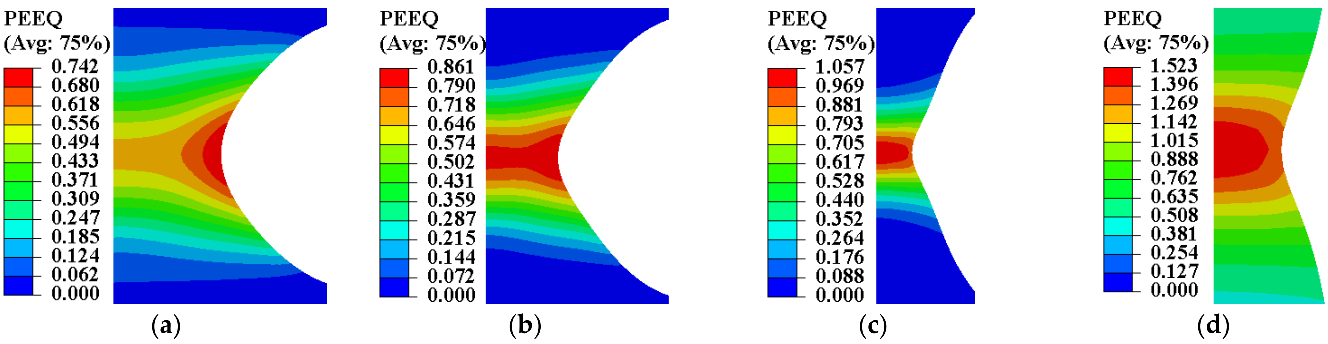

Figure 12. *Cont.*

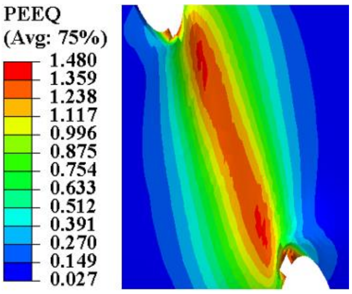

(**e**)

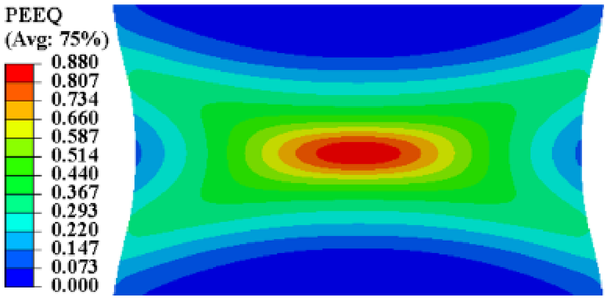

(**f**)

Figure 12. Equivalent plastic strain contours of several mechanical tests: (**a**) R = 2; (**b**) R = 3; (**c**) R = 9; (**d**) R = ∞; (**e**) In-plane shear; (**f**) Plane stress.

Meanwhile, it is well known that the stresses and the two stress state parameters, i.e., the stress triaxiality η and the Lode parameter L, in the specimens vary as plastic deformation occurs. Following the typical method in the literature, we adopted averaged stress state parameters, defined as follows:

$$\overline{\eta}_{\mathrm{av}} = \frac{1}{\varepsilon_{\mathrm{f}}}\int_{0}^{\varepsilon_{\mathrm{f}}} \eta(\varepsilon_{\mathrm{eq}})\mathrm{d}\varepsilon_{\mathrm{eq}},\ \overline{\theta}_{\mathrm{av}} = \frac{1}{\varepsilon_{\mathrm{f}}}\int_{0}^{\varepsilon_{\mathrm{f}}} \overline{\theta}(\varepsilon_{\mathrm{eq}})\mathrm{d}\varepsilon_{\mathrm{eq}}, \tag{11}$$

The stress state parameters and fracture strain values for the SRB (smooth round bar), NRB (notched round bar), in-plane shear, and plane stress test are listed in Table 2.

Table 2. Fracture strain of Q460D steel under different stress states.

Test	Fracture Location	η	L	ε_f
SRB	Centre	0.575	−1	1.523
NRB, R = 2	Centre	1.091	−1	0.742
NRB, R = 3	Centre	0.999	−1	0.861
NRB, R = 9	Centre	0.755	−1	1.057
In-plane shear	Surface	0.0049	−0.0761	1.480
	Mid-surface	0.6147	−0.2099	0.880

Based on the relationship between the fracture strain and the stress triaxiality obtained from the numerical simulations of high-stress triaxiality tests, the stress state term of the MJC fracture criterion was calibrated using Equation (3), and the three parameter values were D_1 = 0.672, D_2 = 9.591, and D_3 = −4.233, as shown in Figure 13.

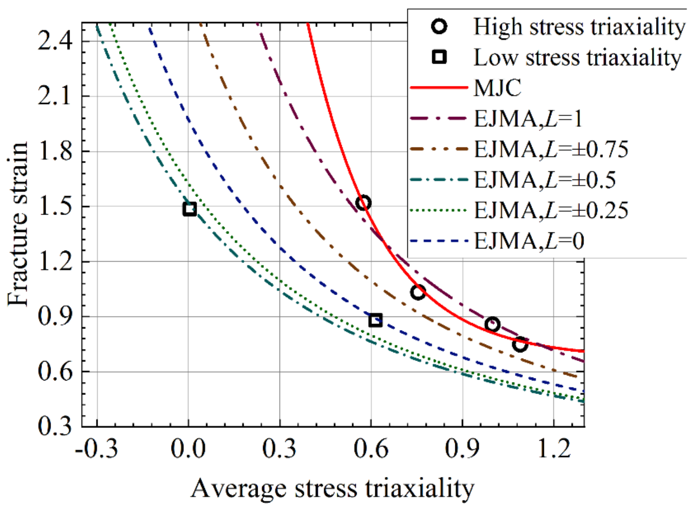

Figure 13. Fracture strain under a complex stress state.

The fitted curve using the MJC fracture criterion was suitable for the high-stress triaxiality state but significantly deviated for the plane strain state, especially for the in-plane shear state. For Q460D steel, it was not sufficient to only consider the effect of the stress triaxiality on the fracture strain, so the lode-dependent EJMA fracture criterion was fitted to the data. The fitted parameter values in Equation (10) were C_1 = 2.956, C_2 = 1.693, and C_3 = 2.06, as shown in Figure 14. Based on the comparison of the fits, the relationship between the fracture strain, lode parameter L, and stress triaxiality η of Q460D steel in different stress states can be better characterized using the EJMA fracture criterion.

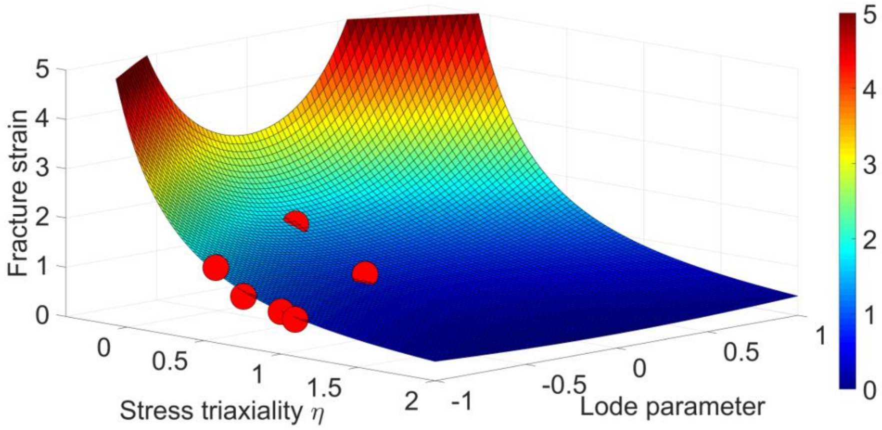

Figure 14. Fracture strain versus stress triaxiality and lode angle simulated using EJMA.

In the calibration of the strain rate parameters, no cracks appeared on the SHPB specimens at different gas pressures, so only the dynamic tensile test results were used. The fractures were clear and easily measured in the recovered specimens in Figure 15, and the fracture strains at different strain rates were calculated as follows:

$$\varepsilon_f = \ln(\frac{A_0}{A_f}), \tag{12}$$

(**a**) (**b**)

Figure 15. Fractured specimens of tensile and dynamic high-temperature tests: (**a**) Dynamic tensile test; (**b**) High-temperature test.

The reference strain rate was 8.333×10^{-4} s^{-1}, which was derived from the smooth tensile tests. The relationship between the fracture strain and strain rate was fitted using Origin software, and the strain rate coefficient D_4 = -0.024 was obtained, as shown in Figure 16.

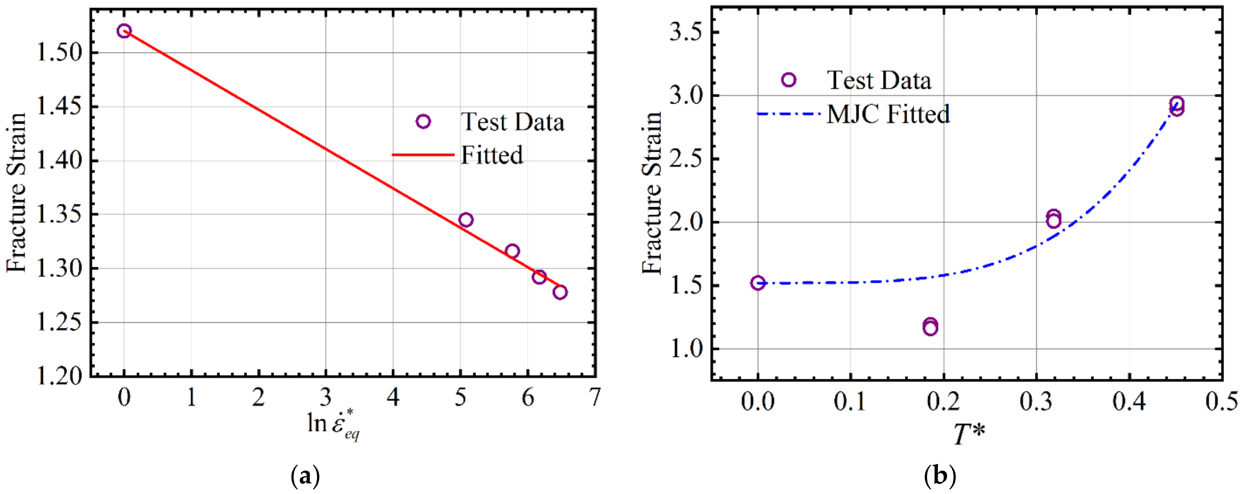

Figure 16. Calibration of strain rate and temperature parameters: (**a**) Relationship between fracture strain and strain rate; (**b**) Relationship between fracture strain and temperature.

The recovered specimens heated at 300 to 700 °C are shown in Figure 15b. A softening effect occurred at 900 °C. The specimen became embedded in the fixture, and secondary damage occurred when the sample was removed, so it was difficult to measure the fracture area accurately. The fracture diameter of each specimen was measured, the temperature parameters were calibrated based on the relationship between the fracture strain and T^*, i.e., the thermal softening coefficients D_5 = 20.3 and D_6 = 3.87 in Equations (3) and (10), as shown in Figure 16b.

Though the nonlinear variation of the Q460D steel with increasing temperature could be well characterized using MJC fracture criterion, the fitting fracture strain at 300 °C was slightly higher than the test value. A blue oxide on the surface of the failure specimen at 300 °C was evident, which indicated the a brittle region formed at this temperature. Consequently, the tensile strength increased, the fracture strain decreased, and the strain became highly time-dependent. Because the strain rate and temperature terms of the MJC fracture criterion are also used in the EJMA fracture criterion, the same coefficients were used. All the material constants are listed in Table 3.

Table 3. Material parameters of Q460D steel.

Description	Notations	Value
Strain constant of MJC constitutive relation	A/MPa	434.63
	B/MPa	666.54
	n	0.577
	α	0.85
	Q/MPa	217.61
	β	16.819
Strain rate constants	C	0.0404
Temperature constants	F	1.777
	m	1.228
EJMA fracture criterion constants	C_1	2.956
	C_2	1.693
	C_3	2.06
MJC fracture criterion constants	D_1	0.672
	D_2	9.591
	D_3	−4.233
	D_4	−0.023
	D_5	20.3
	D_6	3.87

Table 3. *Cont.*

Description	Notations	Value
Others	E/MPa	210
	ν	0.3
	$\rho/(\mathrm{kg/m^3})$	7850
	χ	0.9
	Cp/(J/kg K)	469
	$\dot{\varepsilon}/\mathrm{s}^{-1}$	8.33×10^{-4}
	T_{r}/K	1800
	$T_{\mathrm{m}}/\mathrm{K}$	293

3. Taylor Impact Tests of Q460D Steel

3.1. Test Set-Up

The one-stage light gas gun system of the Nanyang Institute of Technology was used in the tests, as shown in Figure 17. The whole system mainly consisted of a pressurized chamber with a pneumatic device to control the striking velocity, a 1.2 m long and 6 mm caliber diameter launch tube, and a FASTCAMSA-Z high-speed camera that monitored the impact process at 60,000 fps. In addition, it also included flash equipment for the camera, which is not shown in Figure 17. The collection principle is to use the projectile body to pass two laser beams with a known distance to generate an excitation signal to the test device, and to calculate the ejection speed of the projectile through the time difference between the signal generation.

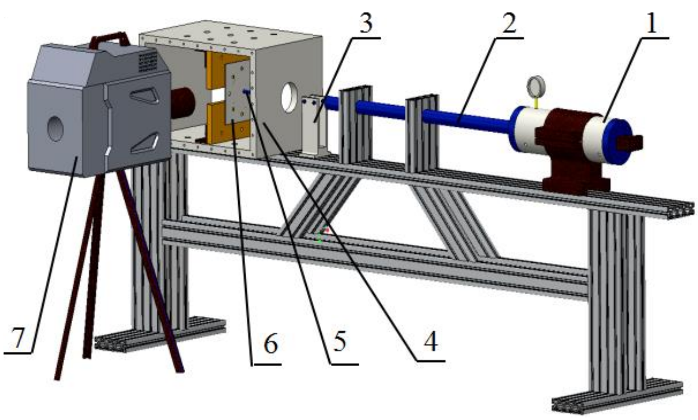

Number	Name
1	Pressurized chamber
2	Launch tube
3	Velocity gauge
4	Impact chamber
5	Projectile
6	Target plate
7	High-speed camera

Figure 17. Schematic diagram of the one-stage light gas gun system.

In the Taylor impact tests, the diameter and length of the Q460D Taylor rod were 5.95 and 29.75 mm, respectively. The target plate was Cr12MnV steel with a hardness of 52 HRC, and it had a diameter and thickness of 55 and 20 mm, respectively, as shown in Figure 18.

The test process and results were mainly analyzed using the PLV software, which was connected to the high-speed camera. The pixel size was calibrated using a Vernier caliper. The projectile was filled into the launch tube and the loading pressure was adjusted based on the desired velocity. After the test, no obvious impact-induced indent on the target plate was evident, and the failure mode of the collected projectile was analyzed. The target was replaced with a new plate for the next test to reduce the error.

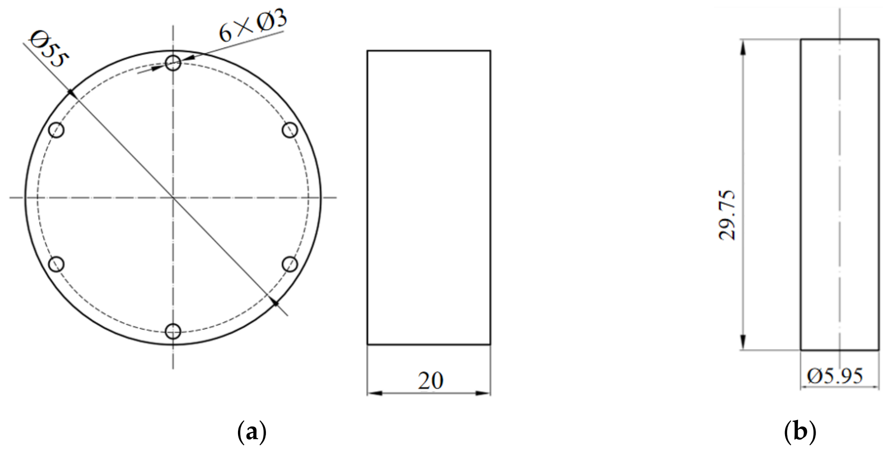

Figure 18. Calibration of strain rate and temperature parameters: (**a**) Relationship between fracture strain and strain rate; (**b**) Projectiles (mm).

3.2. Failure Mode Analysis of Taylor Rods

Through the observation and analysis of all the results, mushrooming, tensile splitting, and petalling failure modes were observed in the nine groups, where the projectile velocity ranged from 191.6 to 422.1 m/s. The measured parameters for each projectile before and after the test are summarized in Table 4. The major and minor axes of the oval-shaped mushrooming failure surface were defined as D_{Lf} and D_{Sf}, respectively, and the equivalent diameter of a circle with the same area as the oval was defined as D_f, respectively.

Table 4. Characteristic size measurements of Q460D steel rod.

Num.	V_0/(m/s)	D_0/mm	L_0/mm	D_{Lf}/mm	D_{Sf}/mm	D_f/mm	L_f/mm	Failure Mode
T1	191.6	5.95	29.76	8.54	8.12	8.33	25.89	Mushrooming
T2	200.0	5.95	29.76	8.75	8.36	8.55	25.59	Mushrooming
T3	238.8	5.95	29.78	9.98	9.38	9.67	24.22	Mushrooming
T4	259.1	5.96	29.75	10.52	9.60	10.09	23.4	Mushrooming
T5	286.1	5.95	29.75	11.28	10.33	10.80	22.68	Mushrooming
T6	326.4	5.94	29.77	/	/	/	21.02	Tensile splitting
T7	372.8	5.95	29.76	/	/	/	19.16	Petalling
T8	378.7	5.95	29.75	/	/	/	18.82	Petalling
T9	422.1	5.95	29.77	/	/	/	16.81	Petalling

Figure 19 shows the mushrooming failure mode of projectiles with impact velocities from 191.6 to 286.1 m/s. Immediately upon impact, the elastic waves and plastic waves are generated at the impact interface. They reflect and propagate in the projectile from the tip to the back, which leads to deceleration and deformation. Due to the target blocking in the axial direction and the deformation developing in the transverse direction, the front part of the projectile bulges out, and mushrooming failure occurs. As the velocity increased, the deformation of the projectile was more significant, which mainly manifested as an increase in the mushrooming surface area and a decrease in the length after the projectile failure. Because the amount of deformation of the projectile at the impact velocity of 286.1 m/s was greater, images of the whole failure process captured by the high-speed camera at this velocity are shown in Figure 20.

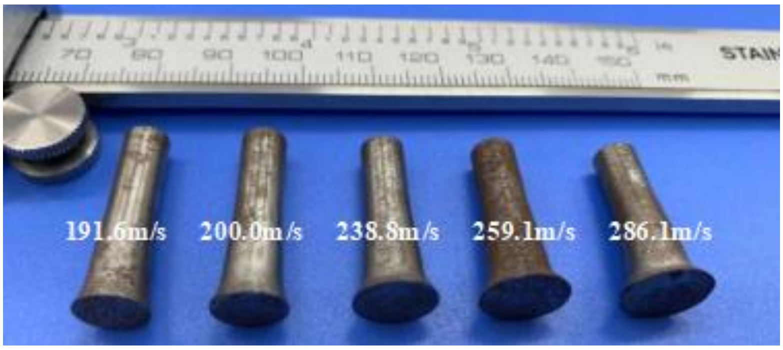

Figure 19. Mushrooming failure of the Taylor specimens.

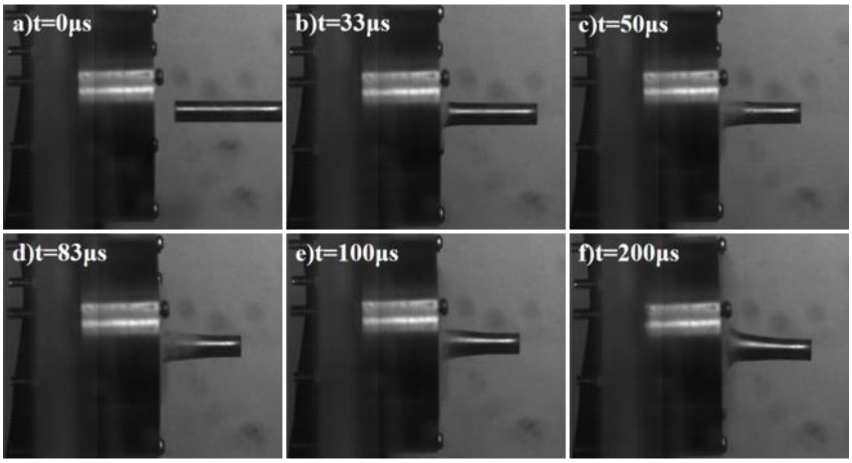

Figure 20. Failure process of Q460D steel rod at V = 286.1 m/s.

With the increase in striking velocity, the mushroomed projectile head localizes the deformation at the tip of the projectile, which causes high hoop strain, which gradually becomes greater than the fracture strain [105]. As shown in Figure 21, a "stagnation region" in the central area of the projectile and few small axial cracks on the edge of the mushrooming area appeared when the impact velocity was 326.4 m/s, and critical tensile splitting nearly occurred. Petalling was observed when the impact velocity was in the range of 372.8–422.1 m/s, and the cracking degree increased as the impact velocity increased. When V = 422.1 m/s, the central area of the mushrooming surface turned blue due to oxidation caused by local adiabatic heating. The whole impact process is shown in Figure 22.

Figure 21. Tensile splitting and petalling process of Taylor specimens.

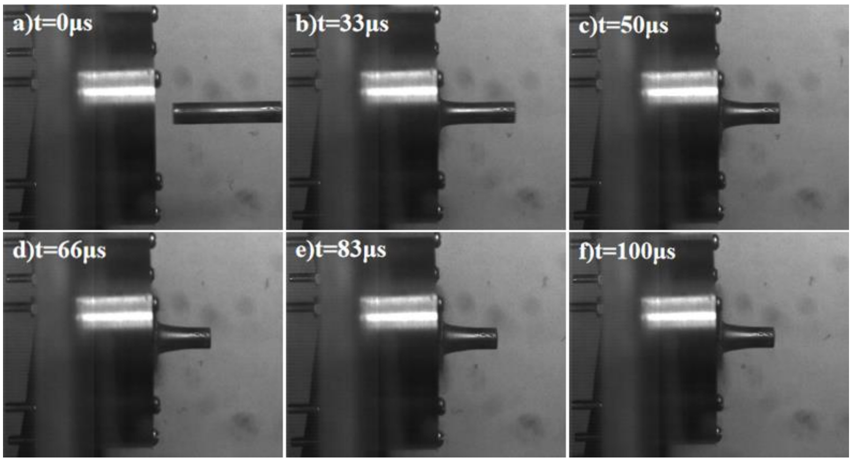

Figure 22. Failure process of Q460D steel rod at V = 422.1 m/s.

4. Numerical Analysis of Taylor Impact Tests

4.1. FE Model Setup

A 3D FE model of the projectile and target plate was built using ABAQUS/Explicit. The diameter and length of projectile were 5.95 and 29.76 mm, respectively, while the diameter and thickness of the target were 55 and 20 mm, respectively. Both were defined as deformable bodies, and the projectile was positioned 0.2 mm above the target plate center. When setting the relative restraint of contacts, the occurrence of fracture and the internal contact of the elastic material after the fracture are considered. A contact pair was set between the outer surface of the projectile and the top surface of the target plate. The contact between the surface of the projectile element was defined to characterize the mechanical behavior of the material during the impact's process. Rigid contact that did not account for the friction during the impact was adopted so that the projectile could be separated from the target after impact, which was similar to the rebound phenomenon of the projectile in the experiments.

C3D8R solid elements were applied for both the projectile and target. The bottom 10 mm of the projectile, which had a complex deformation, was observed. The average element size of this region was 0.2 mm $\times$ 0.2 mm $\times$ 0.25 mm, and the element size gradually increased from 0.25 to 0.6 mm in the length direction to decrease the number of computations for the top area, which only slightly deformed. The target had a higher hardness and deformed imperceptibly during the impact, so the element size in the center was 0.5 mm $\times$ 0.5 mm $\times$ 0.5 mm, and gradually increased to 2 mm $\times$ 2 mm $\times$ 1.96 mm at the edge, as shown in Figure 23. Subsequently, failure deletion and torsion control were added to each element of the target and projectile. The material model parameters of the projectile obtained in Section 3 were input using the tabular method [103], and a bilinear hardening model [55], which could be directly input into ABAQUS, was adopted to express the material properties of the target.

4.2. Predicted Result of FE Simulation

In the velocity range from 191.6 to 286.1 m/s, the numerical result of the mushrooming failure projectile was compared with the test specimen, as shown in Figure 24. The failure mode predicted by the MJC and EJMA fracture criteria was mushrooming failure, which agreed with the test results. The prediction accuracies of the two fracture criteria at medium and low velocities were verified. The comparisons between the numerical and experimental results for the characteristic size of the mushrooming surface and the failure projectile length are listed in Table 5. The numerical result of the characteristic length agreed closely with the experimental values, and all of the errors were less than 5%. The numerical prediction of the characteristic diameter was similar to the test results at low velocities, but the errors were greater than 10% when the impact velocity exceeded 238 m/s. The maximum error reached 12%. Meanwhile, the predicted mushrooming surface was circular, which was different from the elliptical surface of the test specimen. Hence, the influences of anisotropy, the yield plateau, and the strain rate sensitivity should be considered when studying the characteristics of the material plastic flow stress.

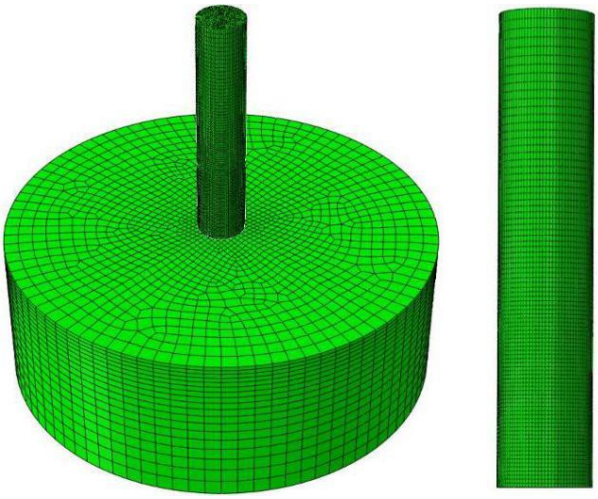

Figure 23. Finite element model of the Taylor impact test.

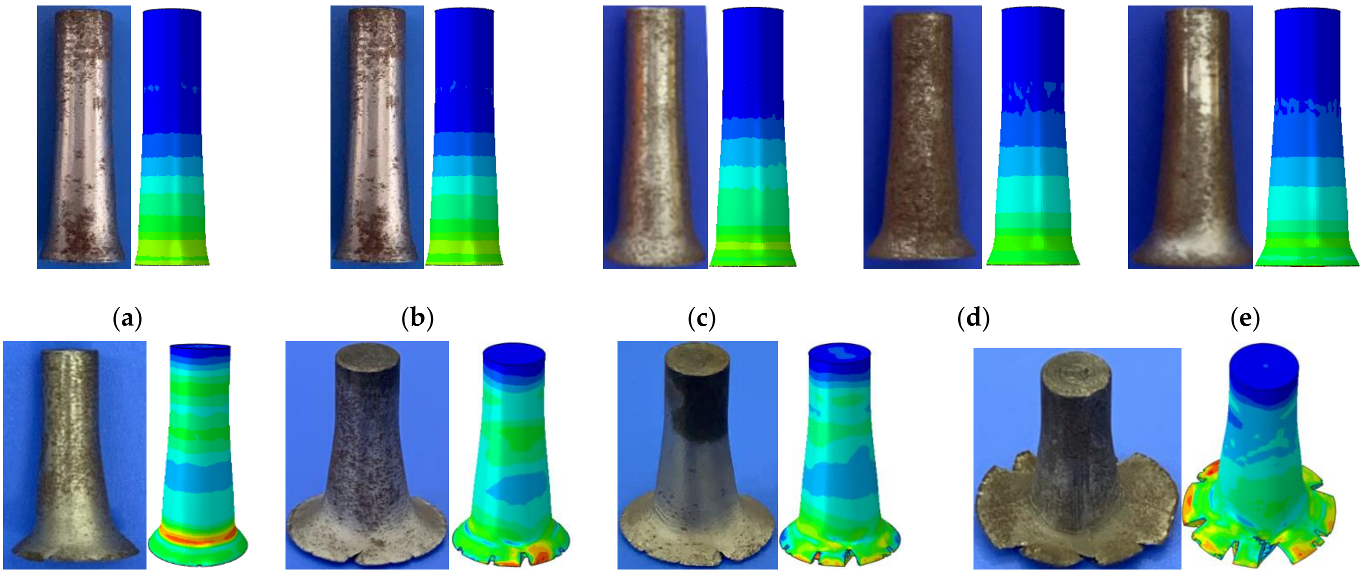

(**a**) (**b**) (**c**) (**d**) (**e**)

(**f**) (**g**) (**h**) (**i**)

Figure 24. Comparison between numerical simulations using EJMA and experimental results at different velocities: (**a**) V = 191.6 m/s; (**b**) V = 200.0 m/s; (**c**) V = 238.8 m/s; (**d**) V = 259.1 m/s; (**e**) V = 286.1 m/s; (**f**) V = 326.4 m/s; (**g**) V = 372.8 m/s; (**h**) V = 378.2 m/s; (**i**) V = 422.1 m/s.

Table 5. Comparison of experimental and numerical mushrooming Taylor rods.

Velocity/(m/s)	Test	FE Simulation		Test	FE Simulation	
	D_f/mm	D_f/mm	Error	L_f/mm	L_f/mm	Error
191.6	8.33	7.67	7.88%	25.89	26.39	1.93%
200.0	8.55	7.81	8.65%	25.59	26.04	1.75%
238.8	9.67	8.48	12.35%	24.22	24.91	2.84%
259.1	10.09	8.89	11.89%	23.40	24.27	3.71%
286.1	10.80	9.48	12.03%	22.68	23.34	2.91%

The critical tensile splitting predicted by the EJMA fracture criterion occurred at a striking velocity of 336 m/s, as shown in Figure 24. The experimental critical velocity was 326.4 m/s, corresponding to a deviation of 2.94%, which was within the allowable margin of error. However, the predicted failure mode of MJC fracture criterion was still mushrooming failure when the striking velocity was 422.1 m/s, which disagreed with the test results. For the three groups of tests in the velocity range from 372.8 to 422.1 m/s, the numerically simulated results of the EJMA fracture criterion were all those of petalling failure. The crack formation and damage degree were similar to the experimental results, as shown in Figure 24.

To explain the discrepancies between the results predicted using the MJC and EJMA fracture criteria, an analysis was conducted based on the stress state of the Taylor rod impact surface material. The damage and stress state value changed the process of the first tensile splitting failure element at the mushrooming surface edge of the critical tensile splitting failure projectile, which was predicted using the EJMA fracture criterion given in Figure 25. The damage mainly appeared between 2.5 and 20 μs. The lode parameter value at this moment was between 0 and -0.25, and the stress triaxiality was between 0 and 0.3. As shown in Figure 13, the fracture strain predicted using the EJMA fracture criterion was far less than that predicted using the MJC fracture criterion. The damage value predicted using the EJMA criterion was higher than that using the MJC fracture criterion, and the amount of damage was greater. Hence, the predicted accuracy of the cracking failure mode at a high striking velocity of a Q460D steel rod could be effectively improved by incorporating the lode angle. As such, the applicability of the EJMA fracture criterion and the validity of the six-parameter calibration was verified.

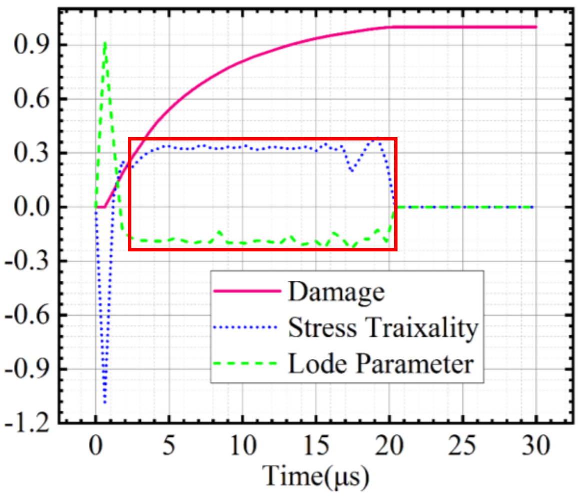

Figure 25. Analysis of damage and stress state.

5. Discussion

In the previous section, the FE simulation results of the Taylor impact tests of Q460D steel rods onto rigid target plates based on the MJC and EJMA fracture criteria were presented. The MJC constitutive relation and the von Mises yield criterion were also applied in the simulation. By comparing the simulated results and the failure mechanisms of the test results at different velocities, it can be seen that the predicted result using the EJMA fracture criterion was significantly better than that using the MJC fracture criterion. This showed that the numerical accuracy of the predictions for the Q460D steel rod failure mode could be effectively enhanced by incorporating the lode angle. Based on the comparison in Table 5, the error of the numerically predicted characteristic diameter of the mushrooming failure at a low striking velocity was still slightly larger, and the maximum error was 12%. Furthermore, there was a significant discrepancy between the circular mushrooming surface of the numerical predictions and the oval surface of the experimental results, and this difference cannot be ignored.

The first possible explanation is that all the specimens used in the materials test were extracted using a Q460D steel plate from the same orientation, and this orientation was defined as 0°. Complex forging and rolling is usually conducted during steel plate metallurgic forming, and thus the mechanical properties in various orientations of the material may differ, i.e., the material could be anisotropic. Hence, the Hill48 yield criterion, which can account for anisotropy, was adopted to characterize the mechanical properties. The Hill48 criterion is as follows:

$$\begin{gathered}F(\sigma_{22}-\sigma_{33})^2+G(\sigma_{33}-\sigma_{11})^2+H(\sigma_{11}-\sigma_{22})^2+\\ 2L\sigma_{23}^2+2M\sigma_{31}^2+2N\sigma_{12}^2-1=0\end{gathered}, \tag{13}$$

where F, G, H, L, M, and N are anisotropic correlation parameters. These parameters can be presented as follows:

$$\begin{cases} F=\frac{1}{2}\left(\frac{1}{R_{22}^2}+\frac{1}{R_{33}^2}-\frac{1}{R_{11}^2}\right), & L=\frac{3}{2}\frac{1}{R_{23}^2} \\ G=\frac{1}{2}\left(\frac{1}{R_{33}^2}+\frac{1}{R_{11}^2}-\frac{1}{R_{22}^2}\right), & M=\frac{3}{2}\frac{1}{R_{13}^2} \\ H=\frac{1}{2}\left(\frac{1}{R_{11}^2}+\frac{1}{R_{22}^2}-\frac{1}{R_{33}^2}\right), & N=\frac{3}{2}\frac{1}{R_{12}^2} \end{cases}, \tag{14}$$

$$\begin{cases} R_{22}=\sqrt{\frac{r_{90}(r_0+1)}{r_0(r_{90}+1)}} \\ R_{33}=\sqrt{\frac{r_{90}(r_0+1)}{r_0+r_{90}}} \\ R_{12}=\sqrt{\frac{3r_{90}(r_0+1)}{(r_{45}+1)+(r_0+r_{90})}} \\ R_{11}=R_{23}=R_{13}=1 \end{cases}, \begin{cases} r_0=\frac{\varepsilon_{yy}}{\varepsilon_{zz}}=\frac{\varepsilon_{yy}}{-(\varepsilon_{xx}+\varepsilon_{yy})} \\ r_{45}=\frac{\varepsilon_{135}}{\varepsilon_{zz}}=\frac{\varepsilon_{135}}{-(\varepsilon_{45}+\varepsilon_{135})} \\ r_{90}=\frac{\varepsilon_{xx}}{\varepsilon_{zz}}=\frac{\varepsilon_{xx}}{-(\varepsilon_{xx}+\varepsilon_{yy})} \end{cases} \tag{15}$$

where R_{ij} is the yield-to-stress ratio corresponding to each orientation of the material axes considered, which can be calculated using the anisotropy index r. The anisotropy indices for the orientations of 0°, 45°, and 90° can be obtained based on the ratio of the plastic strains in the width and thickness orientations during unidirectional tensile tests. The relationship between the plastic strains in the different orientations was observed to satisfy the following equation: ε_{xx} + ε_{yy} + ε_{zz} = 0, where ε_{xx}, ε_{yy}, and ε_{zz} are the plastic strains in the x-, y-, and z-directions, respectively.

Because the anisotropy index should be obtained under unidirectional tensile conditions, three groups of flat dog-bone-shaped (Figure 26) test specimens of the Q460D steel were prepared, and tensile tests at 0°, 45°, and 90° orientations were performed. The conventional specimen extracting orientation is 0°, and the other orientations were defined by rotations from this orientation. The test conditions were similar to those of the notched tensile tests.

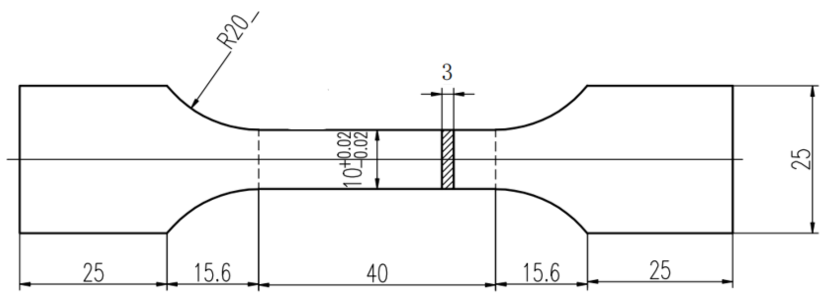

Figure 26. Schematic diagram of a flat dog-bone-shaped specimen.

After the experiments, load–displacement curves were obtained, as shown in Figure 27. The lateral and longitudinal strain of the whole test process were calculated using MatchID-2D software. The analysis was conducted before necking deformation, and the anisotropy indices were r_0 = 0.78, r_{45} = 0.92, and r_{90} = 0.91. The yield-to-stress ratio was calculated using Equation (6), and R_{11} = R_{23} = R_{13} = 1, R_{22} = 1.04, R_{33} = 0.98, and R_{12} = 1.01.

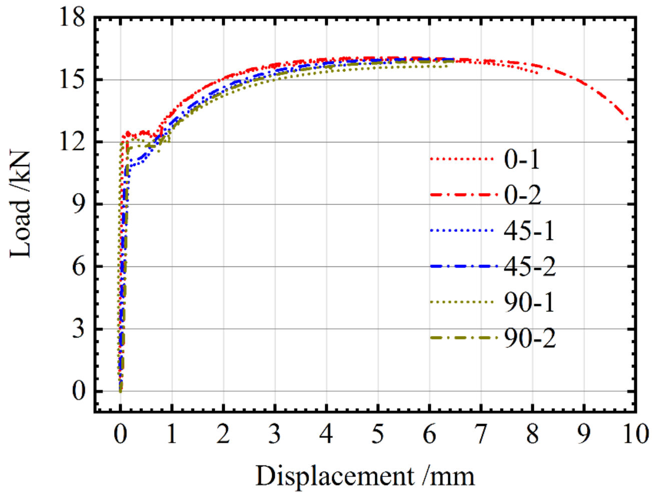

Figure 27. Results of the in-plane tensile tests in different orientations.

However, the adiabatic effect cannot be collocated with the Hill48 yield criterion in ABAQUS FE software, and it was not suitable for the Taylor impact tests, in which the temperature increase is important. An explicit user-defined dynamic material subroutine (VUMAT) based on the Hill48 yield criterion was established. The parameters of the anisotropy yield-to-stress ratio, the constitutive relation, and the fracture criterion were defined in the subroutine, and the specific value was input as an "inp" file. Meanwhile, to facilitate the analysis, the output variables, such as the stress triaxiality, lode angle, and injury were added and output in the form of a solution-dependent variable (SDV). The subroutine was verified by establishing a 3D FE model of the smooth tensile test. The length, width, and thickness directions were defined as the *x*-, *y*-, and *z*-axes. Compared to the experimental results, the numerically predicted oval necking section and output load–displacement curve were similar to the test results, as shown in Figure 28. Thus, the validity of the subroutine was verified.

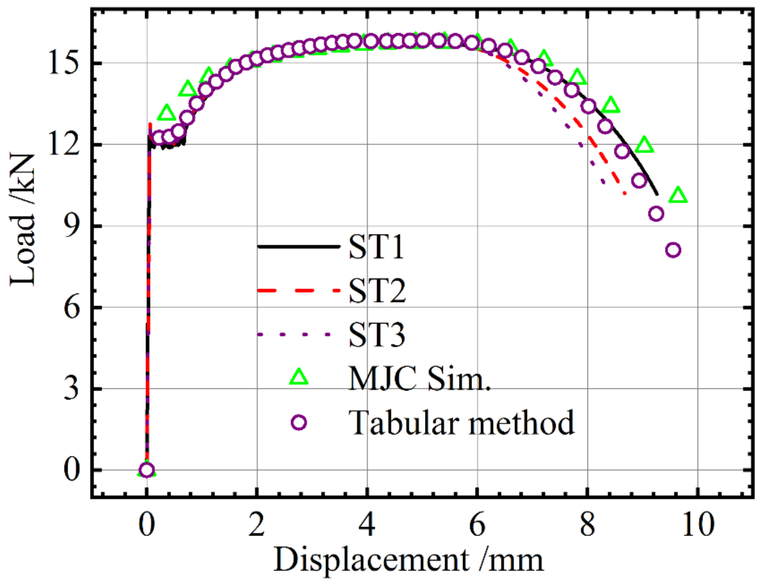

Figure 28. Comparison between FE simulation and experimental results.

Based on the numerical model derived in Section 4, the same material directions were defined, the parameters of the Hill48 yield criterion, MJC constitutive relation, and EJMA fracture criterion of the material model were input into the "inp" document using the Hill48 subroutine, and an SDV item was also added as a field variable. The results of the numerical simulations and experiments are listed in Table 6. The mushrooming surfaces of the numerically predicted result were oval-shaped, similar to the experiments. The predicted error of the characteristic size when $V > 238.8$ m/s changed slightly but was still higher than 10%. Thus, the prediction accuracy of the Taylor rod mushrooming surface shape could be increased effectively by using the Hill48 yield criterion, which accounts for the anisotropy. However, other factors influenced the prediction accuracy of the characteristic size.

Table 6. Simulation results for an anisotropic yield plateau.

Velocity/(m/s)		**191.6**	**200.0**	**238.8**	**259.1**	**286.1**
Test	D_{Lf}/mm	8.54	8.75	9.98	10.52	11.28
	D_{Sf}/mm	8.12	8.36	9.38	9.60	10.33
	L_{f}/mm	25.89	25.59	24.22	23.40	22.68
Anisotropy	D_{Lf}/mm	7.80	7.96	8.65	9.08	9.68
	Error/%	8.66	9.02	13.32	13.68	14.18
	D_{Sf}/mm	7.49	7.63	8.26	8.64	9.20
	Error/%	7.75	8.73	11.94	10.00	10.93
	L_{f}/mm	26.30	26.02	24.90	24.25	23.32
	Error/%	1.58	1.68	2.81	3.63	2.82
Yield plateau	D_{Lf}/mm	7.77	7.93	8.63	9.06	9.67
	Error/%	9.01	9.37	13.52	13.87	14.27
	D_{Sf}/mm	7.46	7.60	8.24	8.63	9.19
	Error/%	8.12	9.09	12.15	10.10	11.04
	L_{f}/mm	26.17	25.89	24.76	24.08	23.14
	Error/%	1.08	1.17	2.22	2.90	2.02
Parameter C	D_{Lf}/mm	8.24	8.42	9.28	9.81	10.55
	Error/%	3.51	3.77	7.01	6.74	6.47
	D_{Sf}/mm	8.12	8.30	9.12	9.62	10.32
	Error/%	0.00	0.71	2.77	0.21	0.09
	L_{f}/mm	25.40	25.08	23.68	22.85	21.82
	Error/%	1.89	1.99	2.23	2.35	3.79
Deformation mechanism	D_{Lf}/mm	8.25	8.44	9.30	9.83	10.61
	Error/%	3.39	3.54	6.81	6.55	5.93
	D_{Sf}/mm	7.91	8.08	8.86	9.32	10.00
	Error/%	2.58	3.34	5.54	2.91	3.19
	L_{f}/mm	26.07	25.78	24.52	23.78	22.84
	Error/%	0.69	0.74	1.23	1.62	0.70

In Figure 28, the load–displacement curve of the test results exhibited yield plateaus at the yield step. However, the yield step curve that was characterized by the strain term showed a rapidly increasing trend, and the characteristic result of the plastic flow stress in this section was significantly higher than the experimental value. Hence, the relationship between the plastic flow stress and the equivalent plastic strain that was obtained using the MJC constitutive relation was discretized using the tabular method. The parameters at the yield section were adjusted and input to the numerical simulation to conduct iterative calculations until the numerical curve coincided with the experimental results, as shown in Figure 28. Isotropic and anisotropic analyses were conducted based on the von Mises and Hill48 yield criteria, respectively. The EJMA fracture criterion and the adjusted constitutive relation were input into the simulations using the tabular method, and the isotropic and anisotropic predictions of the characteristic size are listed in Tables 6 and 7, respectively.

Table 7. Simulation results for the isotropic yield plateau.

Velocity/(m/s)		**191.6**	**200.0**	**238.8**	**259.1**	**286.1**
Test	D_f/mm	8.54	8.75	9.98	10.52	11.28
	L_f/mm	25.89	25.59	24.22	23.40	22.68
Yield plateau	D_{Lf}/mm	7.63	7.78	8.45	8.87	9.47
	Error/%	8.37	9.00	12.66	12.09	12.31
	L_f/mm	26.16	25.89	24.76	24.07	23.12
	Error/%	1.04	1.17	2.23	2.86	1.94
Deformation mechanism	D_{Lf}/mm	8.11	8.28	9.11	9.61	10.35
	Error/%	2.61	3.15	5.84	4.75	4.95
	L_f/mm	26.07	25.77	24.52	23.78	22.81
	Error/%	0.69	0.70	1.23	1.66	0.57

After the yield plateau was characterized reasonably, the predicted mushrooming characteristic sizes for the isotropic and anisotropic materials were similar to the predicted results obtained using the MJC constitutive relation, and the maximum error was also higher than 10%. The predicted characteristic length was better than that obtained using the MJC constitutive relation, the errors decreased by about 30%, and the errors were less than 5%. The characteristic yield plateau was not the main factor that influenced the prediction accuracy of the Taylor impact test.

The strain rate of Taylor impact test can also easily reach 10^4/s to 10^5/s at a low impact velocity, which is far above what the SHPB test can reach, and the variation of the plastic flow stress with strain rate at higher strain rates must be explored. Referring to a previously reported method [1], the value of C was derived based on the mushrooming failure characteristic size at low impact velocities. When C_d = 0.015, the deviations between the numerically predicted characteristic diameter, assuming the material is isotropic at velocities from 191.6 to 286.1 m/s, and the equivalent diameter of the experimental results were all less than 5%. The value of C_d decreased by about 60% from the original value of 0.0404. Subsequently, C_d was adopted to replace the value C. and applied to the analysis of the anisotropy using the Hill48 subroutine. The predicted characteristic sizes for the different velocities are listed in Table 6.

From the comparison with the anisotropic conditions, the predicted errors of the characteristic size were all less than 10%, but the characteristic value of the major axis approached that of the minor axis. The predicted error of the major axis was also much higher than that of the minor axis, so the characteristic shape was disproportional, which was inconsistent with the test results. This illustrated that the predicted accuracy of the Taylor impact tests under anisotropy cannot be enhanced effectively by adjusting the value of C.

Based on the analysis of the SHPB and the dynamic tensile tests in Section 3, the sensitivity of the yield strength to the strain rate at a high strain rate was higher. From the analysis of the dislocation dynamics, the plastic deformation transitioned from a thermally activated mechanism to a phonon drag mechanism, but the transformation of the plastic deformation mechanism was not reasonably considered in the JC constitutive relation. Thus, it was re-expressed based on a previously reported method [106].

The strain terms of the MJC constitutive relation are a linear combination of the Ludwik and Voce laws; thus, they have more parameters. This method is more complex and can easily produce errors. To ensure consistency with the original method, the Ludwik law was applied as the strain term. With parameter A and the temperature fixed, $\sigma_{eq} = \left(A + B\varepsilon_{eq}^{n}\right)(1 + C \ln \varepsilon^{*})$ was adopted to fit the engineering stress–strain curves of the SHPB test at high, medium, and low strain rates, respectively, and the average values B_d = 398.61 MPa and n_d = 0.532 were obtained, as shown in Figure 29. After this, the original strain term was replaced and applied in the FE simulations. Analyses for isotropic and anisotropic materials were conducted, and the predicted characteristic sizes are listed in Tables 6 and 7, respectively.

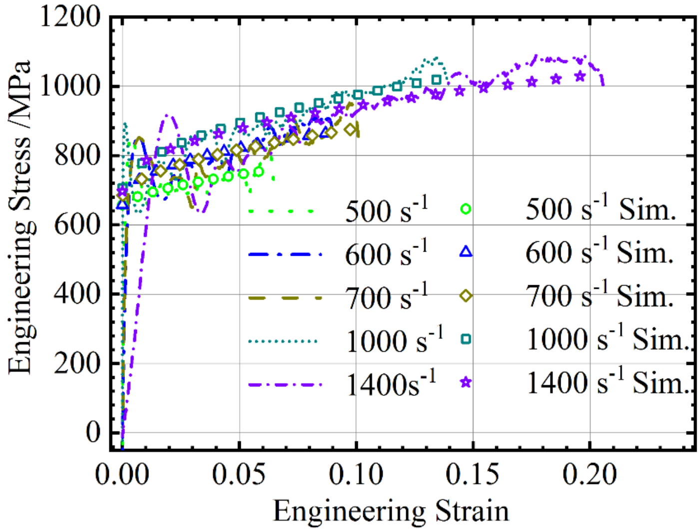

Figure 29. Simulated results at different strain rates.

After considering the effect of the plastic deformation mechanism at high strain rates, the errors of the mushrooming characteristic size for isotropic and anisotropic materials all decreased to about 5%, and the predicted results for the anisotropic conditions were similar to the experiments, as shown in Figure 30. The prediction accuracy increased significantly.

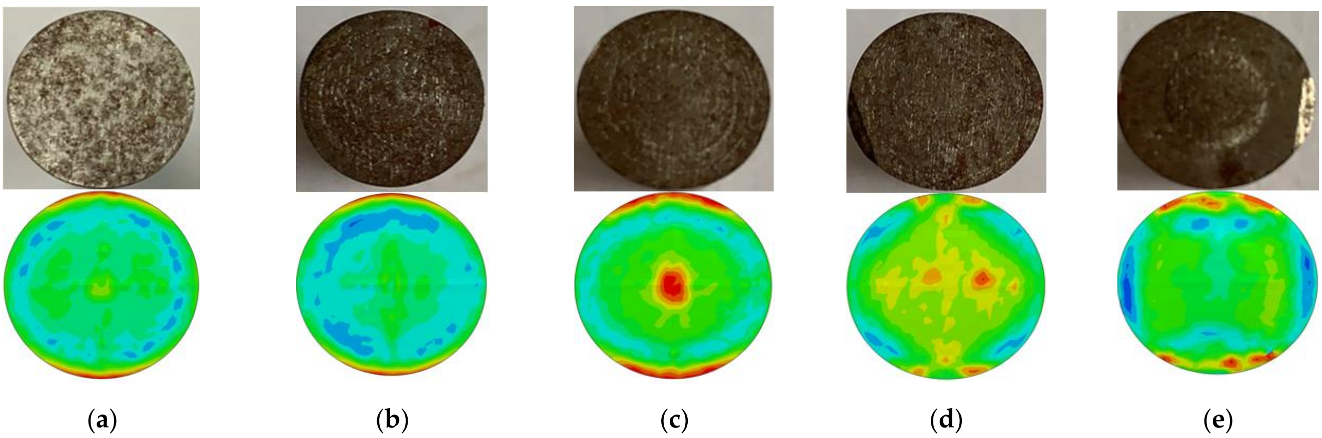

Figure 30. Comparison of the impact surface between the simulation and experiment: (**a**) V = 191.6 m/s; (**b**) V = 200.0 m/s; (**c**) V = 238.8 m/s; (**d**) V = 259.1 m/s; (**e**) V = 286.1 m/s.

The predicted results in the velocity range from 326.4 to 422.1 m/s are shown in Figure 31. In the predicted result at 326.4 m/s, a few slight axial cracks appeared, which was similar to the experiments. Compared to the predicted result using the MJC constitutive relation, which predicted a critical tensile splitting velocity of 336 m/s, the predicted accuracy increased significantly. For the petalling failure mode at higher velocities, the results were similar to the test results in that the damage area was concentrated along the minor axis of the impact surface. The validity of each parameter in the Hill48 yield criterion was verified, and it illustrated that the predicted accuracy of the Taylor impact tests could be increased effectively by considering the lode angle, anisotropy, and strain rate sensitivity.

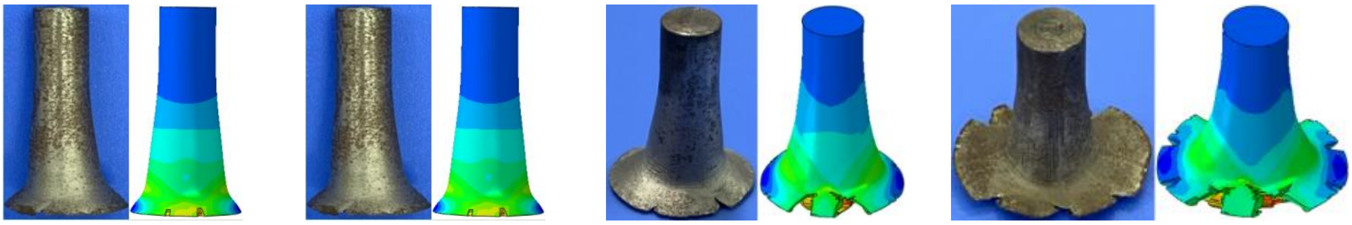
(a) (b) (c) (d)

Figure 31. Prediction results of tensile splitting and petalling process: (**a**) V = 326.4 m/s; (**b**) V = 372.8 m/s; (**c**) V = 378.2 m/s; (**d**) V = 422.1 m/s.

6. Conclusions

In the present work, the material characteristics of Q460D steel were examined by conducting performance tests at different temperatures, strain rates, and stress states. Furthermore, a modified Johnson–Cook (JC) constitutive relation, a modified Johnson-Cook fracture criterion, and a lode-dependent fracture criterion were calibrated using a hybrid experimental–numerical approach. Then, Taylor impact tests of Q460D steel rods onto rigid target plates were performed, and a 3D FE simulation model was developed to analyze the influence of the lode angle on the prediction accuracy for the material fracture behavior. Finally, the influences of the material properties on the prediction accuracy were revealed. The important conclusions are as follows:

1. Based on the analysis of the material tests, the plastic flow stress and fracture strain varied nonlinearly as the temperature increased. To better characterize the strain hardening and thermal softening behavior, the MJC constitutive relation and MJC fracture criterion were adopted and calibrated. Combined with the research into shear and plane strain tests, the lode correlation of the Q460D steel fracturing was studied. The lode-dependent EJMA fracture criterion was calibrated, while the strain rate and temperature terms from the MJC fracture criterion were used.
2. Based on Taylor impact tests of Q460D steel, mushrooming, tensile splitting, and petalling failure modes occurred in the impact velocity range of 191.6–422.1 m/s. Comparing the results predicted using the MJC and EJMA fracture criteria with the experimental results, the failure modes at different striking velocities were well-predicted using the lode-dependent EJMA fracture criterion. Due to a lack of consideration of the Lode angle, the material tenacity was vastly overestimated by the MJC fracture criterion, so that the predicted failure mode at higher velocities did not match that of the experiments. Hence, the prediction accuracy of the cracking failure mode at high striking velocities for the Q460D steel rod could be effectively improved by incorporating the lode angle. Meanwhile, the applicability of the EJMA fracture criterion and the validity of the parameter calibration was verified. However, due to the slightly higher errors of the predicted characteristic sizes at $V > 238.8$ m/s and a characteristic shape prediction that was inconsistent with the experimental results, the effects of anisotropy, the yield plateau, and the strain rate sensitivity should be considered in the FE simulations.
3. In the analysis of the anisotropy, yield plateau, and strain rate sensitivity, the characteristic shape of the projectile impact surface could be better predicted when the Hill48 yield criterion was adopted. The yield plateau was not the main factor. The variation of value C could enhance the predicted characteristic sizes effectively, but was not suitable for anisotropic materials. After considering the effect of the plastic deformation mechanism at high strain rates, the errors of the mushrooming characteristic size under anisotropy all decreased to about 5%, and the predicted elliptical characteristic shape, as well as the failure mode at different impact velocities, was similar to the experimental results. The damaged area of the simulated result was concentrated on the minor axis sides. The validity of each parameter in the Hill48 yield criterion was verified, and it was shown that the predicted accuracy of the Taylor

impact test could be increased effectively by considering the lode angle, anisotropy, and strain rate sensitivity.

Author Contributions: B.H.: Investigation, Conceptualization, Methodology, Formal analysis, Validation Writing—review and editing. T.X.: Investigation, Methodology, Formal analysis, Validation. L.L.: Funding acquisition, Project administration, Supervision, Resources, Investigation, Validation. X.X.: Investigation, Experiment, Formal analysis, Validation, Resources. J.W.: Investigation, Validation. All authors have read and agreed to the published version of the manuscript.

Funding: This research was funded by the Heilongjiang Province Key R & D plan guidance project, and the Tengyi Health City Key project of Excellence and Key technology R & D, grant number GZ20210046; the Science and Technology Department of Henan Province, grant number 222300420505; and the Education Department of Henan Province, grant number 2019GGJS233.

Data Availability Statement: All data are presented in this research.

Conflicts of Interest: The authors declare no conflict of interest.

References

1. Wang, Y.P.; Chen, X.Z.; Xiao, X.K.; Vershinin, V.V.; Ge, R.C.; Li, D.S. Effect of Lode angle incorporation into a fracture criterion in predicting the ballistic resistance of 2024-T351 aluminum alloy plates struck by cylindrical projectiles with different nose shapes. *Int. J. Impact Eng.* **2020**, *139*, 103498. [CrossRef]
2. Malik, A.; Nazeer, F.; Wang, Y.W. A Prospective Way to Achieve Ballistic Impact Resistance of Lightweight Magnesium Alloys. *Metals* **2022**, *12*, 241. [CrossRef]
3. Ganjiani, M.; Homayounfard, M. Development of a ductile failure model sensitive to stress triaxiality and Lode angle. *Int. J. Solids Struct.* **2021**, *225*, 111066. [CrossRef]
4. Bucchi, F.; Frendo, F.; Moreschini, C. Influence of the stress history and of the Lode angle on the determination of the ductile fracture locus for two steel alloys. *Eng. Fract. Mech.* **2022**, *274*, 108759. [CrossRef]
5. Cheng, C.-Q.; Meng, X.-M.; Wu, Y.; Shi, L.-T.; Wu, H.; Cao, T.-S.; Zhang, S.; Zhao, J. On Dynamic Mechanical Properties of 3003 Aluminum Alloy Based on Generalized Incremental Stress-State-Dependent Damage Model with Modified Johnson-Cook Equation. *J. Mater. Eng. Perform.* **2023**, *32*, 451–461. [CrossRef]
6. Lin, L.; Huang, B.; Xiao, X.K.; Huang, M.Y.; Liu, Z.Y. Research on M-Paul Dynamic Constitutive Relation of Q235B Steel. *Adv. Civil Eng.* **2019**, *2019*, 8160283. [CrossRef]
7. Liu, X.; Yan, S.; Rasmussen, K.J.R.; Deierlein, G.G. Experimental investigation of the effect of Lode angle on fracture initiation of steels. *Eng. Fract. Mech.* **2022**, *271*, 108637. [CrossRef]
8. Weber, R.C.; Romero, E.; Lloret, A. Shear strength and yield surface of a partially saturated sandy silt under generalized stress states. *Can. Geotech. J.* **2022**, *59*, 1188–1204. [CrossRef]
9. Yang, H.; Wang, X.; Ni, P.; Li, Z.; Liu, H. Construction of High Strain Rate Loading Constitutive Model and Failure Model and Prediction of Forming Limit for LA103Z Magnesium Alloy. *Met. Mater. Int.* **2022**, *28*, 1938–1947. [CrossRef]
10. You, Q.; Wang, J.-T.; Wu, X.-H.; Sun, Q.; Zhao, B.-Z. Uncoupled fracture model of Q690 high-strength steel based on stress triaxiality and Lode angle parameter. *Fatigue Fract. Eng. Mater. Struct.* **2022**, *45*, 2890–2907. [CrossRef]
11. Rajaraman, D.; Hertele, S.; Fauconnier, D. A novel calibration procedure of Johnson-Cook damage model parameters for simulation of scratch abrasion. *Wear* **2023**, *528*, 204977. [CrossRef]
12. Kachanov, L.M. *On the Time to Rupture under Creep Conditions*; Izv. Akad. Nauk SSSR.: Otdel. Tekhn. Nauk: Moscow, Russia, 1958; Volume 8, pp. 26–31. (In Russian)
13. Rabotnov, Y.N. On the mechanism of long-term fracture. In *Voprosy Prochnosti Materialov i Konstruktsiy*; Reshetov, D.N., Ed.; Izd-vo Akad. Nauk SSSR: Moscow, Russia, 1958; pp. 5–7. (In Russian)
14. Lemaitre, J. *A Course on Damage Mechanics*, 2nd ed.; Springer: Berlin/Heidelberg, Germany; New York, NY, USA, 1996; pp. xix, 210.
15. Lemaitre, J.; Chaboche, J.L.; Benallal, A.; Desmorat, R. *Mechanics of Solid Materials*, 3rd ed.; Dunod: Paris, France, 2009. (In French)
16. Li, S.; Su, Q.; Wang, X.; Wu, Y.; Zhao, X.; Chang, Y. Modification of the Johnson-Cook model for metal at a wide range of strain rates and application in the dynamic response of honeycomb panels. *Model. Simul. Mater. Sci. Eng.* **2022**, *30*, 085012. [CrossRef]
17. Pasco, J.; McCarthy, T.; Parlee, J.; Nazri, N.A.; Padmajan, S.; Rodrigues, S.; Aranas, C., Jr. Constitutive modeling of modified-H13 steel. *MRS Commun.* **2022**, *12*, 343–351. [CrossRef]
18. Vaidogas, E.R. Statistical Analysis of the Dynamic Performance of Reinforcement Steel at Elevated Temperatures: The Case of Johnson-Cook Model. *Mechanika* **2022**, *28*, 19–31. [CrossRef]
19. Wang, Z.; Fu, X.; Xu, N.; Pan, Y.; Zhang, Y. Spatial Constitutive Modeling of AA7050-T7451 with Anisotropic Stress Transformation. *Materials* **2022**, *15*, 5998. [CrossRef]
20. Algarni, M.; Ghazali, S.; Zwawi, M. The Emerging of Stress Triaxiality and Lode Angle in Both Solid and Damage Mechanics: A Review. *Mech. Solids* **2021**, *56*, 787–806. [CrossRef]

21. Peng, Z.; Zhao, H.; Li, X. New ductile fracture model for fracture prediction ranging from negative to high stress triaxiality. *Int. J. Plast.* **2021**, *145*, 103057. [CrossRef]
22. Dou, W.; Xu, Z.; Han, Y.; Huang, F. A ductile fracture model incorporating stress state effect. *Int. J. Mech. Sci.* **2023**, *241*, 107965. [CrossRef]
23. Peng, Z.; Zhao, H.; Li, X.; Yuan, L.; Zhu, T. Ductile fracture of X80 pipeline steel over a wide range of stress triaxialities and Lode angles. *Eng. Fract. Mech.* **2023**, *289*, 109470. [CrossRef]
24. Kolupaev, V.A. Equivalent Stress Concept for Limit State Analysis. In *Advanced Structured Materials*, 1st ed.; Springer International Publishing: Cham, Switzerland, 2018; p. 1.
25. Yu, M.-H. *Unified Strength Theory and Its Applications*, 2nd ed.; Springer: Singapore, 2018; p. 1.
26. Bigoni, D.; Piccolroaz, A. Yield criteria for quasibrittle and frictional materials. *Int. J. Solids Struct.* **2004**, *41*, 2855–2878. [CrossRef]
27. Ehlers, W. A Single-Surface Yield Function for Geomaterials. *Arch. Appl. Mech.* **1995**, *65*, 246–259. [CrossRef]
28. Piccolroaz, A.; Bigoni, D. Yield criteria for quasibrittle and frictional materials: A generalization to surfaces with corners. *Int. J. Solids Struct.* **2009**, *46*, 3587–3596. [CrossRef]
29. Ottosen, N.S. A failure criterion for concrete. *J. Engng. Mech. Div. Proc. ASCE* **1977**, *103*, 527–535. [CrossRef]
30. Mariotte, M. *Treatise on the Movement of Water and Other Fluid Bodies*; Michallet: Paris, France, 1686; pp. XVI, 408, XX. (In French)
31. Timoshenko, S. *History of Strength of Materials, with a Brief Account of the History of Theory of Elasticity and Theory of Structures*; McGraw-Hill: New York, NY, USA, 1953; 452p.
32. Galilei, G. *Discourses and Mathematical Demonstrations Relating to Two New Sciences Related to Mechanics and Local Movements*; Elsevirii: Leida, The Netherlands, 1638; pp. X, 314, VI.
33. Rankine, W.J.M. *A Manual of Applied Mechanics*; R. Griffin: London, UK, 1858; pp. xvi, 640, 8.
34. Coulomb, C.A. Essay on an application of the rules of maxima and minima to some static problems related to architecture. *Mem. Math. Phys. Acad. Roy. Sci. Div. Sav.* **1776**, *7*, 343–387. (In French)
35. Mohr, O. Which factors determine the elastic limit and fracture of a material? *Z. Ver. Dt. Ing.* **1900**, *44*, 1524–1530, 1572–1577. (In German)
36. Tresca, H. A note on the flow of solids subjected to high pressure (in French). *C. R. Acad. Sci. Paris.* **1864**, *59*, 754–758.
37. Tresca, H. A note on the flow of solids. *Mém. Pres. Par. Div. Sav.* **1868**, *18*, 733–799. (In French)
38. Beltrami, E. On the resistance conditions of elastic bodies. *Rend. D. R. Ist. Lomb. Ser. 2* **1885**, *18*, 704–714. (In Italian)
39. Bell, J.F. *The Experimental Foundations of Solid Mechanics*; Springer: Berlin/Heidelberg, Germany; New York, NY, USA, 1984; pp. xii, 813.
40. Huber, M.T. The specific strain work as a measure of the material strength. *Czas. Technol.* **1904**, *22*, 34–40, 49–50, 61–62, 80–81. (In Polish)
41. Von Mises, R. Mechanics of solid bodies in plastically deformable state. *Nachr. Ges. Wiss. Göttingen. Math.-Phys.* **1913**, *1*, 582–592. (In German)
42. Hencky, H. On the theory of plastic deformation and the associated residual strain in the material. *Z. Angew. Math. Mech.* **1924**, *4*, 323–334. (In German) [CrossRef]
43. Sobotka, Z. Theory of plastic flow of anisotropic bodies. *Z. Angew. Math. Mech.* **1969**, *49*, 25–32. (In German) [CrossRef]
44. Karafillis, A.P.; Boyce, M.C. A General Anisotropic Yield Criterion Using Bounds and a Transformation Weighting Tensor. *J. Mech. Phys. Solids* **1993**, *41*, 1859–1886. [CrossRef]
45. Bron, F.; Besson, J. A yield function for anisotropic materials—Application to aluminum alloys. *Int. J. Plast.* **2004**, *20*, 937–963. [CrossRef]
46. Aretz, H.; Barlat, F. New convex yield functions for orthotropic metal plasticity. *Int. J. Nonlin Mech.* **2013**, *51*, 97–111. [CrossRef]
47. Hill, R. A theory of the yielding and plastic flow of anisotropic metals. *Proc. R. Soc. Lond. Ser. A-Math. Phys. Sci.* **1948**, *193*, 281–297.
48. Barlat, F.; Brem, J.C.; Yoon, J.W.; Chung, K.; Dick, R.E.; Lege, D.J.; Pourgoghrat, F.; Choi, S.H.; Chu, E. Plane stress yield function for aluminum alloy sheets—Part 1: Theory. *Int. J. Plast.* **2003**, *19*, 1297–1319. [CrossRef]
49. Banabic, D.; Aretz, H.; Comsa, D.S.; Paraianu, L. An improved analytical description of orthotropy in metallic sheets. *Int. J. Plast.* **2005**, *21*, 493–512. [CrossRef]
50. Barlat, F.; Aretz, H.; Yoon, J.W.; Karabin, M.E.; Brem, J.C.; Dick, R.E. Linear transfomation-based anisotropic yield functions. *Int. J. Plast.* **2005**, *21*, 1009–1039. [CrossRef]
51. Gruzdkov, A.A.; Petrov, Y.V.; Smirnov, V.I. An invariant form of the dynamic criterion for yield of metals. *Phys. Solid State* **2002**, *44*, 2080–2082. [CrossRef]
52. Petrov, Y.V.; Gruzdkov, A.A.; Sitnikova, E.V. Anomalous behavior of yield stress upon an increase in temperature under high strain rate conditions. *Dokl. Phys.* **2007**, *52*, 691–694. [CrossRef]
53. Belytschko, T.; Lin, J.I. A 3-Dimensional Impact Penetration Algorithm with Erosion. *Comput. Struct.* **1987**, *25*, 95–104. [CrossRef]
54. Batra, R.C.; Nechitailo, N.V. Analysis of failure modes in impulsively loaded pre-notched steel plates. *Int. J. Plast.* **1997**, *13*, 291–308. [CrossRef]
55. Borvik, T.; Hopperstad, O.S.; Berstad, T.; Langseth, M. A computational model of viscoplasticity and ductile damage for impact and penetration. *Eur. J. Mech. A-Solid.* **2001**, *20*, 685–712. [CrossRef]

56. Borvik, T.; Clausen, A.H.; Eriksson, M.; Berstad, T.; Hopperstad, O.S.; Langseth, M. Experimental and numerical study on the perforation of AA6005-T6 panels. *Int. J. Impact Eng.* **2005**, *32*, 35–64. [CrossRef]
57. Giglio, M.; Manes, A. Terminal ballistic effect on the crack growth assessment of a helicopter rotor drive. *Eng. Fract. Mech.* **2011**, *78*, 1542–1554. [CrossRef]
58. Fras, T.; Murzyn, A.; Pawlowski, P. Defeat mechanisms provided by slotted add-on bainitic plates against small-calibre 7.62 mm x 51 AP projectiles. *Int. J. Impact Eng.* **2017**, *103*, 241–253. [CrossRef]
59. Jia, B.; Zhang, Y.Y.; Rusinek, A.; Xiao, X.K.; Chai, R.G.; Gu, G.C. Thermo-viscoplastic behavior and constitutive relations for 304 austenitic stainless steel over a wide range of strain rates covering quasi-static, medium, high and very high regimes. *Int. J. Impact Eng.* **2022**, *164*, 104208. [CrossRef]
60. Xiao, X.K.; Shi, Y.H.; Wang, Y.P.; Chen, X.Z.; Jia, B. Effect of incorporating Lode angle parameter into a fracture criterion in predicting ballistic impact behavior of double-layered 2024-T351 aluminum alloy plates against blunt projectiles. *Int. J. Impact Eng.* **2022**, *160*, 104082. [CrossRef]
61. Zhao, Q.; Xiao, X.K.; Ge, R.C.; Zhang, Y.; Chen, X.Z.; Jia, B. Experimental-numerical study on ballistic impact behavior of 316L austenitic stainless steel plates against blunt and ogival projectiles. *Int. J. Hydrogen Energy* **2023**, *48*, 8526–8548. [CrossRef]
62. Shiga, A.; Yamashita, T.; Neishi, Y.; Umezawa, O. Investigation of Ductile Fracture Mechanism in Multipass Drawing of Hollow Specimen. *Mater. Trans.* **2021**, *62*, 505–511. [CrossRef]
63. Qiu, C.-X.; Zhang, A.-F.; Wang, Y.-Z.; Du, X.-L. Study of Ultralow-Cycle Fatigue of Iron-Based SMA in Triaxial Stress States. *J. Mater. Civ. Eng.* **2023**, *35*, 04023347. [CrossRef]
64. Johnson, G.R.; Cook, W.H. A constitutive model and data for metals subjected to large strains, high strain rates and temperatures. In Proceedings of the 7th International Symposium on Ballistics, Hague, The Netherlands, 19–21 April 1983; American Defense Preparedness Association, Koninklijk Instituut van Ingenieurs: Hague, The Netherlands, 1983; pp. 541–547.
65. McClintock, F.A. A criterion for ductile fracture by the growth of holes. *J. Appl. Mech.* **1968**, *35*, 363–371. [CrossRef]
66. Rice, J.R.; Tracey, D.M. On the ductile enlargement of voids in triaxial stress fields. *J. Mech. Phys. Solids* **1969**, *17*, 201–217. [CrossRef]
67. Hancock, J.W.; Mackenzie, A.C. On the mechanisms of ductile failure in high-strength steels subjected to multi-axial stress-states. *J. Mech. Phys. Solids* **1976**, *24*, 147–169. [CrossRef]
68. Bao, Y. Prediction of Ductile Crack Formation in Uncracked Bodies. Ph.D. Thesis, Massachusetts Institute of Technology, Cambridge, MA, USA, 2003.
69. Wierzbicki, T.; Bao, Y.B.; Lee, Y.W.; Bai, Y.L. Calibration and evaluation of seven fracture models. *Int. J. Mech. Sci.* **2005**, *47*, 719–743. [CrossRef]
70. Bai, Y.L.; Wierzbicki, T. A new model of metal plasticity and fracture with pressure and Lode dependence. *Int. J. Plast.* **2008**, *24*, 1071–1096. [CrossRef]
71. Lou, Y.S.; Yoon, J.W.; Huh, H. Modeling of shear ductile fracture considering a changeable cut-off value for stress triaxiality. *Int. J. Plast.* **2014**, *54*, 56–80. [CrossRef]
72. Lou, Y.S.; Chen, L.; Clausmeyer, T.; Tekkaya, A.E.; Yoon, J.W. Modeling of ductile fracture from shear to balanced biaxial tension for sheet metals. *Int. J. Solids Struct.* **2017**, *112*, 169–184. [CrossRef]
73. Lou, Y.S.; Yoon, J.W. Anisotropic ductile fracture criterion based on linear transformation. *Int. J. Plast.* **2017**, *93*, 3–25. [CrossRef]
74. Deng, Y.F.; Hu, A.; Xiao, X.K.; Jia, B. Experimental and numerical investigation on the ballistic resistance of ZK61m magnesium alloy plates struck by blunt and ogival projectiles. *Int. J. Impact Eng.* **2021**, *158*, 104021. [CrossRef]
75. Fan, F.; Xu, T.L.; Zhi, X.D.; Xiao, X.K. Research on dynamic constitutive model and fracture criterion of 6082-T6 aluminium alloy. *Structures* **2022**, *38*, 14–27. [CrossRef]
76. Jia, B.; Rusinek, A.; Xiao, X.K.; Wood, P. Simple shear behavior of 2024-T351 aluminum alloy over a wide range of strain rates and temperatures: Experiments and constitutive modeling. *Int. J. Impact Eng.* **2021**, *156*, 103972. [CrossRef]
77. Santos, I.D.; Sarzosa, D.F.B.; Paredes, M. Ductile fracture modeling using the modified Mohr-Coulomb model coupled with a softening law for an ASTM A285 steel. *Thin-Walled Struct.* **2022**, *176*, 109341. [CrossRef]
78. Shi, Y.H.; Hu, A.; Du, T.S.; Xiao, X.K.; Jia, B. Experimental and Numerical Study on the Protective Behavior of Weldox 900 E Steel Plates Impacted by Blunt-Nosed Projectiles. *Metals* **2022**, *12*, 141. [CrossRef]
79. Barlat, F.; Lege, D.J.; Brem, J.C. A 6-Component Yield Function for Anisotropic Materials. *Int. J. Plast.* **1991**, *7*, 693–712. [CrossRef]
80. Vasco, M.C.; Tserpes, K.; Pantelakis, S.G. Numerical Simulation of Tensile Behavior of Corroded Aluminum Alloy 2024 T3 Considering the Hydrogen Embrittlement. *Metals* **2018**, *8*, 56. [CrossRef]
81. Gilmour, K.R.; Leacock, A.G.; Ashbridge, M.T.J. The influence of plastic strain ratios on the numerical modelling of stretch forming. *J. Mater. Process Tech.* **2004**, *152*, 116–125. [CrossRef]
82. Seidt, J.D. Plastic Deformation and Ductile Fracture of 2024-T351 Aluminum under Various Loading Conditions. Ph.D. Thesis, The Ohio State University, Columbus, OH, USA, 2010.
83. Papasidero, J.; Doquet, V.; Mohr, D. Ductile fracture of aluminum 2024-T351 under proportional and non-proportional multi-axial loading: Bao-Wierzbicki results revisited. *Int. J. Solids Struct.* **2015**, *69–70*, 459–474. [CrossRef]
84. Zhou, L.; Wen, H.M. A new Dynamic Plasticity and Failure Model for Metals. *Metals* **2019**, *9*, 905. [CrossRef]

85. Han, J.; Shi, Y.H.; Ma, Q.Q.; Vershinin, V.V.; Chen, X.Z.; Xiao, X.K.; Jia, B. Experimental and numerical investigation on the ballistic resistance of 2024-T351 aluminum alloy plates with various thicknesses struck by blunt projectiles. *Int. J. Impact Eng.* **2022**, *163*, 104182. [CrossRef]
86. Vershinin, V.V. A correct form of Bai-Wierzbicki plasticity model and its extension for strain rate and temperature dependence. *Int. J. Solids Struct.* **2017**, *126*, 150–162. [CrossRef]
87. Vershinin, V.V. Validation of metal plasticity and fracture models through numerical simulation of high velocity perforation. *Int. J. Solids Struct.* **2015**, *67–68*, 127–138. [CrossRef]
88. Wen, H.J.; Mahmoud, H. New Model for Ductile Fracture of Metal Alloys. I: Monotonic Loading" by Huajie Wen and Hussam Mahmoud. *J. Eng. Mech.* **2016**, *142*, 04015088. [CrossRef]
89. Yao, Z.C.; Wang, W.; Kanvinde, A. A constitutive model of cyclic plasticity with Lode dependence for structural steels. *Comput. Struct.* **2022**, *268*, 106826. [CrossRef]
90. Yang, X.Q.; Yang, H.; Zhang, S.M. Rate-dependent constitutive models of S690 high-strength structural steel. *Constr. Build. Mater.* **2019**, *198*, 597–607. [CrossRef]
91. Cowper, G.R.; Symonds, P.S. *Strain-Hardening and Strain-Rate Effects in the Impact Loading of Cantilever Beams*; Brown University: Providence, RI, USA, 1957; 46p.
92. Johnson, G.R.; Cook, W.H. Fracture characteristics of three metals subjected to various strains, strain rates, temperatures and pressures. *Engng. Fract. Mech.* **1985**, *21*, 31–48. [CrossRef]
93. Jiang, J.; Ye, M.; Chen, L.Y.; Zhu, Z.; Wu, M. Study on static strength of Q690 built-up K-joints under axial loads. *Structures* **2023**, *51*, 760–775. [CrossRef]
94. Tian, L.M.; Li, M.H.; Li, L.; Li, D.Y.; Bai, C. Novel joint for improving the collapse resistance of steel frame structures in column-loss scenarios. *Thin-Walled Struct.* **2023**, *182*, 110219. [CrossRef]
95. Huang, H.; Yao, Y.F.; Liang, C.J.; Ye, Y.X. Experimental study on cyclic performance of steel-hollow core partially encased composite spliced frame beam. *Soil. Dyn. Earthq. Eng.* **2022**, *163*, 107499. [CrossRef]
96. Wu, S.T.; Zhou, C.W.; Shi, Y.H.; Hu, A.; Xiao, X.K. Plasticity, ductile fracture and ballistic impact behavior of Ti-6Al-4V Alloy. *Int. J. Impact Eng.* **2023**, *174*, 104493. [CrossRef]
97. Deng, Y.F.; Wu, H.P.; Zhang, Y.; Huang, X.L.; Xiao, X.K.; Lv, Y.H. Experimental and numerical study on the ballistic resistance of 6061-T651 aluminum alloy thin plates struck by different nose shapes of projectiles. *Int. J. Impact Eng.* **2022**, *160*, 104083. [CrossRef]
98. Lin, L.; Zhi, X.; Fan, F. Determination of parameters of Johnson-Cook models of Q235B steel. *J. Vib. Shock.* **2014**, *33*, 153–158+172. (In Chinese)
99. Sung, J.H.; Kim, J.N.; Wagoner, R.H. A plastic constitutive equation incorporating strain, strain-rate, and temperature. *Int. J. Plast.* **2010**, *26*, 1746–1771. [CrossRef]
100. Xiao, X.K.; Mu, Z.C.; Pan, H.; Lou, Y.S. Effect of the Lode parameter in predicting shear cracking of 2024-T351 aluminum alloy Taylor rods. *Int. J. Impact Eng.* **2018**, *120*, 185–201. [CrossRef]
101. Ludwik, P. *Elemente der Technologischen Mechanik*; Springer: Berlin/Heidelberg, Germany, 1909.
102. Voce, E. The relationship between stress and strain for homogeneous deformations. *J. Inst. Metals* **1948**, *74*, 537–562.
103. Xiao, X.K. *The Ballistic Resistance of Double-Layered Metallic Target and the Deformation & Fracture of Taylor Rod*; Harbin Institute of Technology: Harbin, China, 2010. (In Chinese)
104. Odeshi, A.G.; Al-ameen, S.; Bassim, M.N. Effect of high strain rate on plastic deformation of a low alloy steel subjected to ballistic impact. *J. Mater. Process Tech.* **2005**, *162*, 385–391. [CrossRef]
105. Xiao, X.K.; Zhang, W.; Wei, G.; Mu, Z.C. Effect of projectile hardness on deformation and fracture behavior in the Taylor impact test. *Mater. Des.* **2010**, *31*, 4913–4920. [CrossRef]
106. Guo, Z.T.; Shu, K.G.; Gao, B.; Zhang, W. J-C model based failure criterion and verification of Q235 steel. *Explos. Shock. Waves* **2018**, *38*, 1325–1332. (In Chinese)